Potential of electrical resistivity tomography to infer aquifer transport characteristics from tracer studies: A synthetic case study

Jan Vanderborght, Andreas Kemna, Horst Hardelauf, and Harry Vereecken

Agrosphere Institute, ICG-IV, Forschungszentrum Jülich GmbH, Jülich, Germany

Received 29 October 2004; revised 17 March 2005; accepted 29 March 2005; published 21 June 2005.

[1] With time-lapse electrical resistivity tomography (ERT), transport processes in the subsurface can be imaged and monitored. The information content of obtained spatiotemporal data sets opens new ways to characterize subsurface spatial variability. Difficulties regarding a quantitative interpretation of the imaged transport may arise from the fact that data inversion used in ERT is generally underdetermined and that ERT data acquisition is often limited to two-dimensional (2-D) image planes. To address this problem, we conducted a numerical tracer experiment in a synthetic heterogeneous aquifer with preset variability and spatial correlation of the hydraulic conductivity and monitored the tracer breakthrough in a 2-D image plane perpendicular to the mean flow direction using time-lapse ERT. The tracer breakthrough patterns in the image plane were interpreted using equivalent transport models: an equivalent convection dispersion equation to characterize the spatially averaged breakthrough and a stream tube model to characterize local breakthrough curves. Equivalent parameters derived from simulated and from ERT inverted concentrations showed a good agreement, which demonstrates the potential of ERT to characterize subsurface transport. Using first-order approximate solutions of stochastic flow and transport equations, equivalent model parameters and their spatial variability were interpreted in terms of the local-scale dispersion and the spatial variability of the hydraulic conductivity. The spatial correlations of the stream tube velocity and of the hydraulic conductivity were found to be closely related. Consequently, the hydraulic conductivity spatial correlation may be inferred from stream tube velocity distributions, which can be observed with sufficiently high spatial resolution using ERT.

Citation: Vanderborght, J., A. Kemna, H. Hardelauf, and H. Vereecken (2005), Potential of electrical resistivity tomography to infer aquifer transport characteristics from tracer studies: A synthetic case study, *Water Resour. Res.*, *41*, W06013, doi:10.1029/2004WR003774.

1. Introduction

[2] Tomographic geophysical techniques are attractive for characterizing the structure and heterogeneity of the subsurface since spatially continuous images of subsurface properties can be obtained with minimal disturbance. Flow and transport processes are strongly determined by the structure and heterogeneity of subsurface transport properties, especially the hydraulic conductivity. Therefore geophysical methods are increasingly being used in hydrogeological studies and the field of "hydrogeophysics" is emerging [*Hubbard and Rubin*, 2004]. Geophysical methods map the spatial distribution of geophysical parameters. Using petrophysical relations between geophysical and hydrological parameters [e.g., *Slater and Lesmes*, 2002; *Lesmes and Friedman*, 2004], hydraulic structures may be derived directly. More sophisticated methods making use of geostatistical techniques have been developed to combine geophysical and hydrological data of different spatial support and to characterize subsurface structure in either a direct or geostatistical way [e.g., *Rubin et al.*, 1992; *Ezzedine et al.*, 1999; *Hubbard et al.*, 1999; *Purvance and Andricevic*, 2000].

[3] Besides imaging of "static" subsurface structures, geophysical methods have also been used to monitor subsurface flow and transport processes. A number of studies have illustrated the potential of ERT for monitoring tracer experiments in soils [e.g., *Binley et al.*, 1996, 2002; *Slater et al.*, 1997; *French et al.*, 2002] and aquifers [e.g., *Slater et al.*, 2000; *Kemna et al.*, 2002; *Singha et al.*, 2003]. The spatiotemporal information that is obtained using ERT monitoring can be used to calibrate flow and transport models. *Binley et al.* [2002] estimated the effective hydraulic conductivity from a controlled water infiltration test in the vadose zone that was monitored using cross-borehole ERT and transmission radar tomography. *Kemna et al.* [2002] estimated effective dispersivity and tracer velocities from a salt tracer breakthrough that was monitored across a reference plane using cross-borehole ERT.

[4] However, for a quantitative interpretation of ERT images in terms of hydraulic and transport parameters, two aspects need further consideration. First, ERT represents an inherently nonunique inverse problem. Usually, a

0043-1397/05/2004WR003774

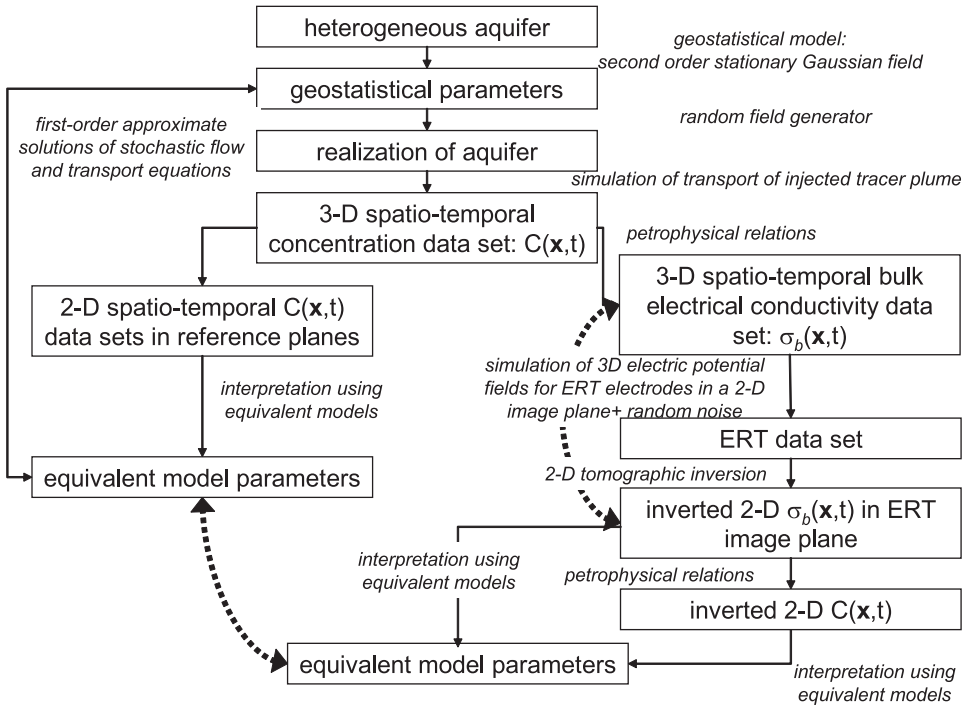

Figure 1. Information flowchart. Data sets and parameters are shown in boxes, and operations performed on a data/parameter set are represented by italicized text. Thick dashed lines represent comparisons between information derived from ERT data sets and from simulated concentration or bulk electrical conductivity data sets.

regularization term is added to the data misfit term in the objective function to constrain the inversion problem. A variety of regularization terms can be used and their choice is not based on the ERT data but on other a priori information, best guesses, and/or experience. Because of limited data acquisition and computational resources, ERT data are commonly collected along a 2-D profile or image plane and then inverted assuming that the medium is invariant in the third direction. As a consequence, both the 2-D representation of an actually 3-D distribution of electrical subsurface properties and the required regularization term lead to an uncertainty in the inverted image which is not generated by data error or noise. *Kemna et al.* [2002] illustrated the effect of using different regularizations on estimated equivalent transport parameters for a regular 2-D tracer distribution. However, their analysis did not take into account the 2-D approximation of a 3-D conductivity distribution.

[5] Second, transport parameters that are derived from 2-D ERT images are equivalent parameters of models which represent a simplification of the heterogeneous 3-D flow and transport process. A characterization of the subsurface hydraulic property distribution based on ERT monitored tracer experiments requires therefore a relationship between equivalent transport parameters and the spatial distribution of the hydraulic properties. The actual or conditioned spatial distribution of the hydraulic properties in the tracer test area can be inferred from measured hydraulic state variables and equivalent transport parameters using an inversion of the 3-D flow and transport equations [e.g., *Harvey and Gorelick*, 1995; *Yeh and Simunek*, 2002]. However, since the process that is observed in a 2-D image plane perpendicular to the mean flow direction represents the lumped result of a 3-D transport process between the injection and image plane, a 3-D inversion based on basically 2-D lumped information is prone to be underdetermined. Rather than attempting to derive the actual spatial distribution of the hydraulic properties, the geostatistical parameters that characterize this spatial distribution in a stochastic framework could be derived from equivalent transport parameters observed in a 2-D image plane. Relationships between equivalent transport parameters and geostatistical parameters have been derived using first-order approximate solutions of the stochastic flow and transport equations. The variance dissipation of local concentrations or the dilution [e.g., *Kapoor and Kitanidis*, 1998; *Pannone and Kitanidis*, 1999; *Fiori and Dagan*, 2000; *Cirpka and Kitanidis*, 2000; *Vanderborght and Vereecken*, 2002], the spatial correlation of particle arrival times on a reference plane [*Rubin and Ezzedine*, 1997; *Vanderborght and Vereecken*, 2001; *Bellin and Rubin*, 2004], and the spatial covariance of the concentration field [*Vanderborght*, 2001] were related to the spatial covariance of the hydraulic conductivity field and the local-scale dispersion. Information about travel time distributions and spatial covariances of travel times was used by, for example, *Woodbury and Rubin* [2000], *Vanderborght and Vereecken* [2001, 2002], and *Bellin and Rubin* [2004] to infer geostatistical parameters and local-scale dispersion from tracer tests. In these studies, tracer breakthrough was measured using multilevel groundwater samplers. However, because of sparse sampling in the horizontal direction, the spatial resolution that can be obtained with these methods is limited so that the inferred correlation scale in the flow direction is uncertain.

[6] The overall objective of this study is to investigate the potential of ERT to obtain spatiotemporal information about tracer transport across a reference plane in a heterogeneous aquifer and to illustrate how this information can be used to characterize aquifer heterogeneity in terms of geostatistical parameters. We conducted a numerical tracer experiment in a synthetic heterogeneous aquifer with a preset variability and spatial correlation structure of the hydraulic conductivity and monitored the tracer breakthrough across a 2-D image plane perpendicular to the mean flow direction using time-lapse ERT. The tracer breakthrough patterns on reference planes are parameterized using equivalent transport models. First-order approximate solutions of stochastic flow and transport equations are used to interpret these equivalent parameters in terms of the local-scale dispersion and the spatial variability of the hydraulic conductivity. An information flowchart showing the links between different data and parameter sets and the operations performed on them is given in Figure 1.

2. Theory

2.1. Three-Dimensional Flow and Transport Equations

[7] Assuming a sink/source free domain and an incompressible medium, the hydraulic head distribution in an aquifer is obtained by solving the 3-D flow equation for given boundary conditions:

$$\nabla \cdot (K_s(\mathbf{x})\nabla\psi(\mathbf{x})) = 0 \tag{1}$$

where $K_s(\mathbf{x})$ is the hydraulic conductivity, which is assumed to be isotropic at the local scale and represented by a scalar, and $\psi(\mathbf{x})$ is the hydraulic head. From the hydraulic head field, the Darcy flow velocity, $\mathbf{q}(\mathbf{x})$, is derived:

$$\mathbf{q}(\mathbf{x}) = -K_s(\mathbf{x})\nabla\psi(\mathbf{x}) \tag{2}$$

Transport of a nonreactive tracer in the 3-D flow field $\mathbf{q}(\mathbf{x})$ is described using the convection dispersion equation (CDE):

$$\phi_0 \frac{\partial C(\mathbf{x},t)}{\partial t} = -\mathbf{q}(\mathbf{x})\nabla C(\mathbf{x},t) + \nabla \cdot (\phi_0 \mathbf{D_d}(\mathbf{x})\nabla C(\mathbf{x},t)) \tag{3}$$

where $C(\mathbf{x}, t)$ is the solute concentration in the liquid phase, and $\mathbf{D_d}(\mathbf{x})$ is the local-scale dispersion tensor and ϕ_0 is the water filled pore space which we assume to be constant in space. According to *Bear* [1972], the entries of the dispersion tensor can be expressed as

$$D_{d,ij}(\mathbf{x}) = \delta_{ij}\tau(\phi_0)D_0 + \delta_{ij}\lambda_{dT} \parallel \mathbf{u} \parallel + (\lambda_{dL} - \lambda_{dT})\frac{u_i u_j}{\parallel \mathbf{u} \parallel} \tag{4}$$

where δ_{ij} is the Kronecker delta, $\tau(\phi_0)$ is a tortuosity factor, D_0 the molecular diffusion constant, $\mathbf{u}$ the pore water velocity ($\mathbf{u} = \mathbf{q}/\phi_0$), and λ_{dL} and λ_{dT} the longitudinal and transverse dispersivities, respectively.

2.2. Representation of Heterogeneity

[8] Since the deterministic spatial distribution of hydraulic conductivity, K_s, is generally not known, it is regarded as a stochastic parameter and its spatial variation is expressed in a geostatistical framework. Several data sets suggest that the distribution of K_s is described by a lognormal distribution [e.g., *Gelhar*, 1993]. The spatial variability of $\log_e K_s(\mathbf{x})$ is represented by a random space function which is assumed to be a second-order stationary Gaussian random field, i.e., the expected value and the two point covariance of $\log_e K_s(\mathbf{x})$, are defined and translation invariant:

$$\langle \log_e K_s(\mathbf{x}) \rangle = \langle \log_e K_s(\mathbf{x}') \rangle \equiv F \tag{5}$$

$$\begin{aligned}\langle (\log_e K_s(\mathbf{x}) - F)(\log_e K_s(\mathbf{x}+\mathbf{h}) - F) \rangle &\equiv \langle f(\mathbf{x}) f(\mathbf{x}+\mathbf{h}) \rangle \\ &= \langle f(\mathbf{x}') f(\mathbf{x}'+\mathbf{h}) \rangle \equiv C_{ff}(\mathbf{h})\end{aligned} \tag{6}$$

where $\langle y \rangle$ represents the expected value of the random variable in all realizations, $\mathbf{h}$ is the separation lag, and $C_{ff}(\mathbf{h})$ is the spatial covariance of the $\log_e K_s$ or its perturbation f. An exponential covariance function $C_{ff}(\mathbf{h})$ is assumed:

$$C_{ff}(\mathbf{h}) = \sigma_f^2 \exp\left(-\sqrt{\left(\frac{h_1}{\gamma_1}\right)^2 + \left(\frac{h_2}{\gamma_2}\right)^2 + \left(\frac{h_3}{\gamma_3}\right)^2}\right) \tag{7}$$

where σ_f^2 is the variance of the $\log_e K_s$ and γ_i the correlation length in direction i.

2.3. Equivalent Transport Models and Parameters

[9] The 3-D transport process in a heterogeneous aquifer may be represented using equivalent transport models and model parameters. This representation serves two purposes. The first is to upscale the transport process to a larger scale where local variations of advection velocities cannot be considered. The second is to quantify the spatial variability of the transport.

[10] Two equivalent transport models are considered. The first is the "upscaled" or "equivalent" convection dispersion model which describes ensemble averaged concentrations, $\langle C(\mathbf{x}, t) \rangle$, i.e., the expected concentration in all realizations of the conductivity field. This model assumes a hydrodynamically uniform medium with a large-scale deterministic and uniform advection velocity $\mathbf{U}$ and equivalent dispersion tensor $\mathbf{D}_{\mathrm{eq}}$. Ensemble averaged concentrations are described as

$$\frac{\partial \langle C(\mathbf{x},t) \rangle}{\partial t} = -\mathbf{U}\nabla \langle C(\mathbf{x},t) \rangle + \mathbf{D_{eq}}\nabla^2 \langle C(\mathbf{x},t) \rangle \tag{8}$$

[11] Similar to the difference between flux and resident concentrations in homogenous media, the ensemble averaged concentration can be defined in two ways: either $\langle C(\mathbf{x}, t) \rangle$ represents the average of the local concentrations in all realizations, i.e., the ensemble resident or volume averaged concentration $\langle C^r(\mathbf{x}, t) \rangle$, or $\langle C(\mathbf{x}, t) \rangle$ represents the average of the local solute fluxes divided by the average of the local water fluxes, i.e., the ensemble flux averaged concentration $\langle C^f(\mathbf{x}, t) \rangle$ which is defined as

$$\langle C^f(\mathbf{x},t) \rangle \equiv \frac{\langle q_{1s}(\mathbf{x},t) \rangle}{\langle q_1(\mathbf{x}) \rangle} \approx \frac{\langle q_1(\mathbf{x}) C(\mathbf{x},t) \rangle}{\langle q_1(\mathbf{x}) \rangle} \tag{9}$$

where q_{1s} and q_1 are, respectively, the solute and water flux in direction x_1. The approximation in equation (9) implies the assumption of advection dominated transport character-

ized by large Peclet numbers, i.e., Pe = $x_1/\lambda_{dL} \gg 10$ (x_1 is the transport distance), so that the local dispersive solute flux can be neglected compared with the advective solute flux component [*Parker and van Genuchten*, 1984], which is generally valid in aquifers. $\langle C^r(\mathbf{x}, t)\rangle$ is related to a solute particle location probability distribution whereas $\langle C^f(\mathbf{x}, t)\rangle$ relates to a distribution of particle travel times. When the hydraulic conductivity field is stationary, when the mean or expected flow field is uniform, and when the extent of the solute plume in the direction perpendicular to the mean flow direction is much larger than the spatial correlation scale of the hydraulic conductivity, $\langle C(\mathbf{x}, t)\rangle$ is constant in a plane perpendicular to the mean flow direction (i.e., $\langle C(\mathbf{x}, t)\rangle = \langle C(x_1, t)\rangle$ where x_1 is the flow direction). Then the ensemble averaged concentration, $\langle C(x_1, t)\rangle$, can be represented by the spatial average of the local concentrations/solute fluxes in that plane. Since we inject a tracer plume in a wide injection slab perpendicular to the mean flow direction (see below), we assume that these assumptions are met in our study and we interchange in the following the expected value ($\langle\ \rangle$) of a variable in all realizations of the hydraulic conductivity field with the spatial average of the variable in a plane perpendicular to the mean flow direction. Under these conditions the large-scale transport process can be represented as a one dimensional process and the equivalent convection-dispersion model, equation (8) can be written as

$$\frac{\partial\langle C(x_1,t)\rangle}{\partial t} = -U_1\frac{\partial\langle C(x_1,t)\rangle}{\partial x_1} + \lambda_{eq}U_1\frac{\partial^2\langle C(x_1,t)\rangle}{\partial x_1^2} \tag{10}$$

where U_1 is the mean pore water velocity and λ_{eq} is the equivalent dispersivitiy that is defined as $\lambda_{eq} = D_{1eq}/U_1$ and quantifies the spreading of averaged 1-D concentration profiles or of averaged breakthrough curves. Only for large travel distances, relative to the correlation of the hydraulic conductivity, equation (10) can predict the evolution of concentration profiles and breakthrough curves with time and depth using a constant λ_{eq}. For smaller travel distances, the equivalent convection dispersion model and λ_{eq} must be interpreted as tools to describe and parameterize an observed breakthrough curve (BTC) that is assumed to be the result of a 1-D equivalent convection dispersion process in a hydrodynamically homogeneous medium. For small travel distances, the spreading of concentration profiles and breakthrough curves increases more rapidly with increasing travel distance than predicted by an equivalent convection-dispersion model assuming a constant λ_{eq}. As a consequence, λ_{eq} derived from breakthrough curves at different travel distances increases with travel distance.

[12] The second equivalent model that describes and parameterizes time series of locally observed concentrations is the stream tube model (STM). A time series of solute concentrations at a certain point, $C(\mathbf{x}, t)$, is interpreted as the result of a 1-D convection dispersion process in a stream tube, which connects the injection plane with $\mathbf{x}$. Transport in the stream tube is described as

$$\frac{\partial C(\xi,t)}{\partial t} = -v_s(\mathbf{x})\frac{\partial C(\xi,t)}{\partial \xi} + v_s(\mathbf{x})\lambda_s(\mathbf{x})\frac{\partial^2 C(\xi,t)}{\partial \xi^2} \tag{11}$$

where $v_s(\mathbf{x})$ and $\lambda_s(\mathbf{x})$ are the stream tube velocity and dispersivity, respectively, and ξ is the stream tube coordinate. When the stream tube is assumed to be a straight tube, ξ corresponds with the coordinate of the mean flow direction, x_1. Similar to the equivalent dispersion model, the stream tube model must be interpreted as a tool to parameterize a local BTC that is observed at a certain location $\mathbf{x}$ assuming a 1-D transport process in a hydrodynamically homogeneous and isolated stream tube. The stream tube velocity $v_s(\mathbf{x})$ represents the average velocity of particles along their trajectory from the injection plane to point $\mathbf{x}$. The spatial variability of $v_s(\mathbf{x})$ in a reference plane perpendicular to the mean flow direction reflects the spatial variability of the flow. The stream tube dispersivity, $\lambda_s(\mathbf{x})$, is a measure of the dilution of the injected concentration due to local mixing processes along the stream tube trajectory between the injection plane and $\mathbf{x}$.

[13] For an instantaneous injection of solutes across an injection plane perpendicular to the mean flow direction, the time series of $\langle C^f(x_1, t)\rangle$ and $C(\mathbf{x}, t)$ represent solute travel time distributions from the injection plane to the reference plane and the observation point $\mathbf{x}$, respectively. The equivalent model parameters can be derived from the temporal moments of the travel time distributions: the average arrival time, $\overline{\tau}(x_1)$ or $\overline{\tau}(\mathbf{x})$, and the variance of arrival times, $\sigma_\tau^2(x_1)$ or $\sigma_\tau^2(\mathbf{x})$ [e.g., *Jury and Sposito*, 1985]:

$$U_1(x_1) = \frac{x_1}{\overline{\tau}(x_1)} = \frac{x_1}{\int_0^\infty t\langle c^f(x_1,t)\rangle dt} \tag{12}$$

$$v_s(\mathbf{x}) = \frac{x_1}{\overline{\tau}(\mathbf{x})} = \frac{x_1}{\int_0^\infty tc(\mathbf{x},t)dt} \tag{13}$$

$$\lambda_{eq}(x_1) = \frac{x_1\sigma_\tau^2(x_1)}{2\overline{\tau}^2(x_1)} = \frac{U_1^2\left[\int_0^\infty t^2\langle c^f(x_1,t)\rangle dt - \left(\int_0^\infty t\langle c^f(x_1,t)\rangle dt\right)^2\right]}{2x_1} \tag{14}$$

$$\lambda_s(\mathbf{x}) = \frac{x_1\sigma_\tau^2(\mathbf{x})}{2\overline{\tau}^2(\mathbf{x})} = \frac{v_s^2(\mathbf{x})\left[\int_0^\infty t^2c(\mathbf{x},t)dt - \left(\int_0^\infty tc(\mathbf{x},t)dt\right)^2\right]}{2x_1} \tag{15}$$

where $\langle c^f(x_1, t)\rangle$ and $c(\mathbf{x}, t)$ are time normalized concentrations:

$$\langle c^f(x_1,t)\rangle = \frac{\langle C^f(x_1,t)\rangle}{\int_0^\infty \langle C^f(x_1,t)\rangle dt} \tag{16}$$

$$c(\mathbf{x},t) = \frac{C(\mathbf{x},t)}{\int_0^\infty C(\mathbf{x},t)dt} \tag{17}$$

As an alternative, the analytical solution of the CDE for a Dirac $\delta(t)$ uniform solute flux at the injection plane and assuming no backward diffusion across the injection plane (i.e., a semi-infinite medium), which leads to the same relations between temporal moments of concentrations and CDE parameters, can be fitted to time series of local or averaged concentrations:

$$\langle c(x_1,t)\rangle = \frac{x_1}{\sqrt{4\pi\lambda_{eq}U_1t^3}}\exp\left[-\frac{(x_1-U_1t)^2}{4\lambda_{eq}U_1t}\right] \tag{18}$$

$$c(\mathbf{x},t) = \frac{x_1}{\sqrt{4\pi\lambda_s(\mathbf{x})v_s(\mathbf{x})t^3}}\exp\left[-\frac{(x_1-v_s(\mathbf{x})t)^2}{4\lambda_s(\mathbf{x})v_s(\mathbf{x})t}\right] \tag{19}$$

2.4. First-Order Predictions of Equivalent Transport Parameters and Their Spatial Variability

[14] The equivalent parameters can be predicted in terms of geostatistical parameters, which characterize the spatial variability of the hydraulic conductivity, and the local-scale solute transport parameters, which describe local-scale processes such as local-scale hydrodynamic dispersion.

[15] Because $K_s(\mathbf{x})$ is a stochastic parameter, the pore water velocity $\mathbf{u}(\mathbf{x})$ and the concentration $C(\mathbf{x}, t)$ are random variables and the flow (equation (1)) and transport (equation (3)) equations are stochastic equations. In the Lagrangian approach, the transport equation is interpreted as an equation that describes the probability distribution of locations or of arrival times of individual solute particles. The moments of the particle location and arrival time distributions are derived from the kinematic equations that describe the particle trajectories. The travel time, τ, of a particle from an injection point $\mathbf{a}$ to a reference plane at distance x_1 from the injection plane is given as [*Dagan et al.*, 1992]

$$\frac{d\tau(x_1;\mathbf{a})}{dx_1} = \frac{1}{u_1(\mathbf{X}(\tau;\mathbf{a})) + v_{d1}(\tau)} \tag{20}$$

where u_1 is the pore water velocity in the direction of the mean flow, $\mathbf{X}(\tau;\mathbf{a})$ is the location of the particle at time τ, and $v_{d1}(\tau)$ is a velocity fluctuation which represents the effect of the local-scale dispersion process. Equation (20) forms the basis for the derivation of the moments of the particle arrival times from the statistics of the pore water velocity and the local-scale dispersion. The particle trajectory, along which the pore water velocities need to be evaluated, depends implicitly on the stochastic velocity field so that it is generally not possible to obtain explicit relations between the particle travel time statistics and the statistics of the velocity field. In order to solve this problem, the particle trajectory is approximated by the expected trajectory [e.g., *Dagan*, 1989], $\langle\mathbf{X}(\tau;\mathbf{a})\rangle = \mathbf{U}\,\tau + \mathbf{a}$, and a deviation that accounts for the displacement due to local-scale dispersive velocities, $\mathbf{x_d}(t) = \int_0^t \mathbf{v_d}(t')dt'$ [*Fiori and Dagan*, 2000]. Furthermore, the approximate solutions are obtained assuming that the local-scale dispersion tensor, $\mathbf{D_d}$, and the porosity, ϕ_0, are constant. The derivation of the first-order estimate of the variance of arrival times at a reference plane, $\sigma_\tau^2(x_1)$, is given, for instance, by *Vanderborght and Vereecken* [2002]. Combining equation (13) of *Vanderborght and Vereecken* [2002] (and correcting it for a typographical error) with equation (14) above, the first-order estimate of the equivalent dispersivity is given by

$$\lambda_{eq}(x_1) \approx \lambda_L + \frac{1}{x_1}\int_0^{x_1/U_1}\int_0^t\int_{\mathbf{k}} \exp\left[\left(ik_1U_1 - \mathbf{k^T}\cdot\mathbf{D_d}\cdot\mathbf{k}\right)(t-t')\right] \cdot S_{u_1u_1}(\mathbf{k})d\mathbf{k}dt'dt \tag{21}$$

where $\mathbf{S_{uu}(k)}$ is the first-order approximation of the spectrum of the local-scale velocity field, which is related to the spatial covariance of the velocity field, $C_{\mathrm{uiuj}}(\mathbf{h})$, as

$$C_{u_iu_j}(\mathbf{h}) = \left\langle\left(u_i(\mathbf{x})-U_i\right)\left(u_j(\mathbf{x}+\mathbf{h})-U_j\right)\right\rangle = \int_{-\infty}^{+\infty}\exp[i\mathbf{k}\cdot\mathbf{h}]S_{u_iu_j}(\mathbf{k})d\mathbf{k} \tag{22}$$

For the longitudinal (i.e., in the flow direction) component of the local velocity (u_1) and an exponential covariance function of $\log_e K_s$, the first-order approximate velocity spectrum, $S_{u1u1}(\mathbf{k})$, is given by [e.g., *Russo*, 1995]

$$S_{u_1u_1}(\mathbf{k}) \approx \left[1-\frac{k_1^2}{k_1^2+k_2^2+k_3^2}\right]^2\frac{U_1^2\sigma_f^2\gamma_1\gamma_2\gamma_3}{\pi^2\left(1+\gamma_1^2k_1^2+\gamma_2^2k_2^2+\gamma_3^2k_3^2\right)^2} \tag{23}$$

[16] The expected variance of arrival times at a certain point on the reference plane for a given realization of the velocity field, $\langle\sigma_\tau^2(\mathbf{x})\rangle$, is obtained by subtracting the covariance of arrival times of two different particles that cross the reference plane at the same point, $\sigma_{\tau\tau}(\mathbf{x}, \mathbf{x})$, from the variance of particle arrival times at the reference plane, $\sigma_\tau^2(x_1)$. The covariance of arrival times $\sigma_{\tau\tau}(\mathbf{x}, \mathbf{x})$ is given in equation (17) of *Vanderborght and Vereecken* [2002]. The first-order approximation of the expected stream tube dispersivity $\langle\lambda_s(x_1)\rangle$ is

$$\langle\lambda_s(x_1)\rangle \approx \lambda_{eq}(x_1) - \frac{1}{2x_1}\int_0^{x_1/U_1}\int_0^{x_1/U_1}\int_{\mathbf{k}}\exp \cdot\left[ik_1U_1(t-t') - \mathbf{k^T}\cdot\mathbf{D_d}\cdot\mathbf{k}(t+t')\right]S_{u_1u_1}(\mathbf{k})\mathbf{dk}dtdt' \tag{24}$$

In a first-order approximation, the spatial covariance of stream tube velocities, $C_{v_sv_s}(\mathbf{x}, \mathbf{x}+\mathbf{h})$, is related to the two-particle arrival time covariance $\sigma_{\tau\tau}(\mathbf{x}, \mathbf{x}+\mathbf{h})$ as (see Appendix A)

$$C_{v_sv_s}(\mathbf{x},\mathbf{x}+\mathbf{h}) \approx \frac{U_1^4}{x_1^2}\sigma_{\tau\tau}(\mathbf{x},\mathbf{x}+\mathbf{h}) \tag{25}$$

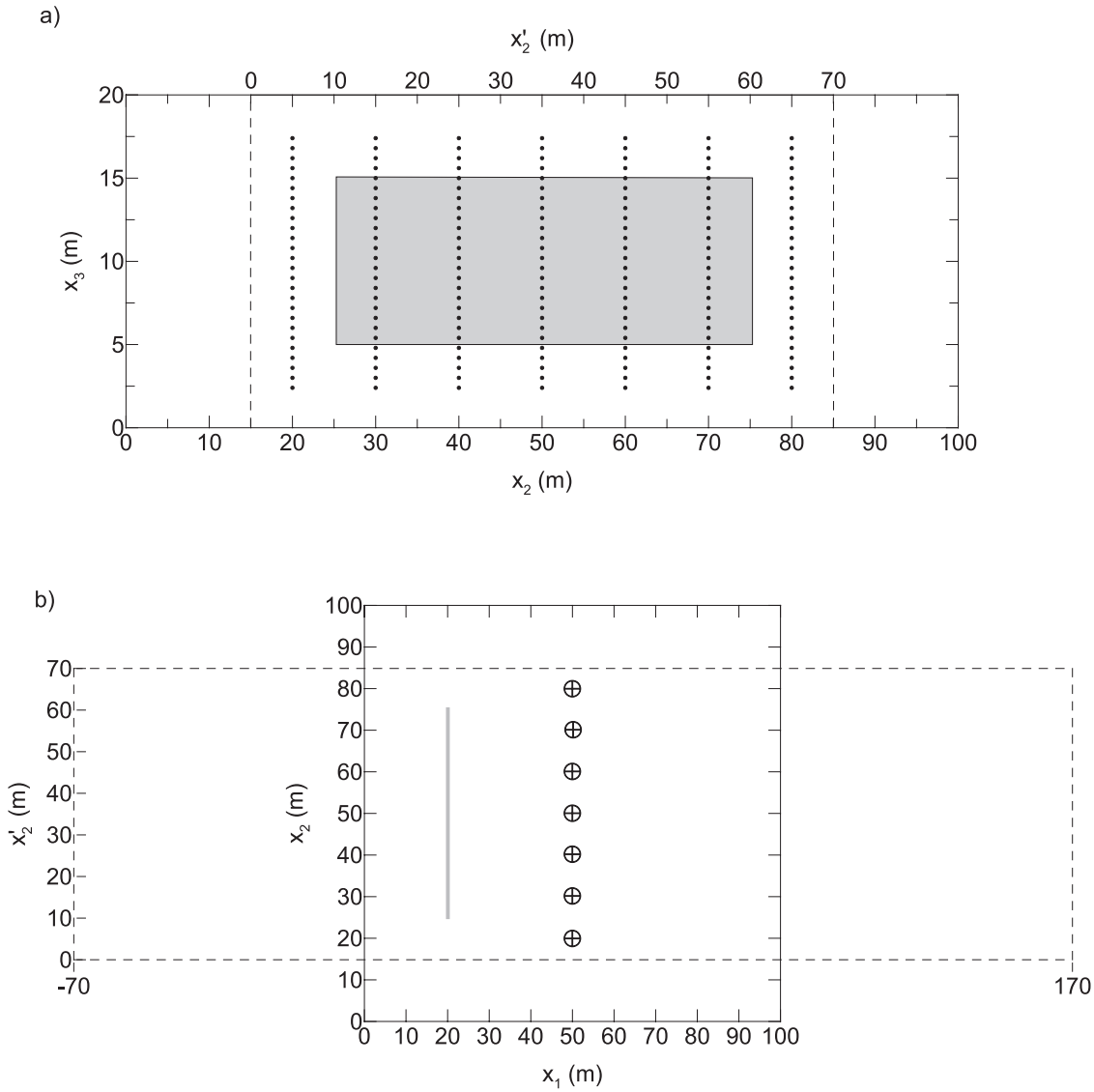

Figure 2. (a) Frontal and (b) top view of the hydraulic (solid lines) and electric (dashed lines) simulation domains, the coordinate systems, the location of the electrodes (solid circles), of the boreholes (circled crosses), and of the solute injection slab (shaded line or rectangle).

The first-order approximation of the two-particle arrival time covariance is given as

$$\sigma_{\tau\tau}(\mathbf{x},\mathbf{x}+\mathbf{h}) \approx \frac{1}{U_1^2}\int_0^{x_1/U_1}\int_0^{x_1/U_1}\int_{\mathbf{k}} \exp \cdot \left[ik_1U_1(t-t') + i\mathbf{k}\cdot\mathbf{h} - \mathbf{k}^{\mathbf{T}}\cdot\mathbf{D_d}\cdot\mathbf{k}(t+t')\right]S_{u_1u_1}(\mathbf{k})\mathbf{dk}dtdt' \tag{26}$$

The number of multiple integrals in equations (21), (24), and (26) was first reduced by elementary calculus (equations (21) and (24) reduce to equations (A15) and (A16) of *Vanderborght and Vereecken* [2002], respectively) and the resulting integrals were evaluated numerically.

3. Methods

[17] In this part, the setup of the numerical experiment and the derivation of equivalent parameters from simulated breakthrough curves are presented. A scheme of the electric and hydraulic simulation domains, the locations of the electrodes, bore holes, and the solute injection slab is given in Figure 2. The flow and transport parameters and the setup of the ERT data acquisition were chosen so as to represent realistic conditions. The 3-D flow and transport simulations and the 3-D modeling of the electric potential fields were carried out on the Cray T3E supercomputing system at the Forschungszentrum Jülich whereas the 2-D ERT inversions were performed on a standard PC.

3.1. Setup of Flow and Transport Simulation

[18] An aquifer model with a heterogeneous distribution of $K_s(\mathbf{x})$ was generated using a Kraichnan random field generator [*Kraichnan*, 1970]. The spatial correlation of $\log_e K_s$ was assumed to be isotropic in the horizontal direction, i.e., $\gamma_1 = \gamma_2$. The porosity, ϕ_0, of the flow domain was set equal to 0.25. An overview of the used flow and transport parameters, the preset geostatistical parameters, as well as the actual mean and variance of the generated

Table 1. Parameters of the Flow and Transport Models: Geometric Mean of the Hydraulic Conductivity (K_g), Porosity (ϕ_0), Longitudinal (λ_{dL}) and Transverse (λ_{dT}) Dispersivity, and Geostatistical Parameters of the Exponential Covariance Model, Variance (σ_f^2) and Correlation Length (γ_i) of Log_e Transformed Hydraulic Conductivity[a]

Parameter	Value
Flow and transport parameters	
K_g, m d^{-1}	250 (239.2)
ϕ_0	0.25
λ_{dL}, m	0.1
λ_{dT}, m	0.01
Geostatistical parameters	
σ_f^2	1.0 (1.02)
γ_1, m	5
γ_2, m	5
γ_3, m	1

[a]See equation (7). Parameters in parentheses are the actual mean and variance of the generated conductivity field.

conductivity field are shown in Table 1. The dimensions of the simulation domains L_i and the grid sizes Δx_i are given in Table 2. The preset spatial correlation function, $\rho_{ff}(\mathbf{h}) = C_{ff}(\mathbf{h})/C_{ff}(\mathbf{0})$, and the spatial correlation of the generated hydraulic conductivity field are shown in Figure 3.

[19] At the bottom and top boundaries ($x_3 = 0$ and $x_3 = L_3 = 20$ m) and at the two lateral boundaries ($x_2 = 0$ and $x_2 = L_2 = 100$ m), a zero flow or zero hydraulic head gradient boundary condition was implemented. At the front and back surfaces ($x_1 = 0$ and $x_1 = L_1 = 100$ m), a uniform hydraulic head distribution was defined so that the mean hydraulic head gradient in the x_1 direction was -0.001. The hydraulic head and Darcy flow velocity fields were obtained by a numerical solution of equation (1) using the 3-D finite element code TRACE [*Vereecken et al.*, 1994].

[20] For the transport simulations, we assumed that the molecular diffusion can be neglected. The longitudinal and transverse dispersivities (equation (4)) were defined as 0.1 m (λ_{dL}) and 0.01 m (λ_{dT}), respectively. These local-scale dispersivities are larger than dispersivity values reported for sandy aquifers (e.g., $\lambda_{dT} = 0.005$ m by *Fiori and Dagan* [1999] for the Borden test site) but of the same order of magnitude as dispersivity lengths that were derived from an analysis of local breakthrough curves observed in a gravel sediment [e.g., *Vanderborght and Vereecken*, 2002]. To solve the transport equation (equation (3)) zero flux boundary conditions were imposed on the lateral, top and bottom, and front boundaries. A uniform initial tracer concentration C_0 was assumed in a 50 m wide, 10 m deep and 0.5 m thick vertical slab at 20 m downstream from the front boundary ($x_1 = 20$ m) in the region 25 m $< x_2 <$ 75 m and 5 m $< x_3 <$ 15 m. An initially solute free domain was defined outside the injection slab. The transport equation was numerically solved for these initial and boundary conditions using the PARTRACE code [*Neuendorf*, 1997], which solves the convection dispersion equation using a particle tracking procedure. 10^8 particles were "injected" which corresponds to 10^4 particles per grid cell of the injection slab. In the PARTRACE code, the advective movement of individual particles in the flow field is tracked and local-scale dispersion is modeled by adding a random displacement. Concentration distributions were calculated until 150 days after tracer injection at daily intervals by counting the number of particles in the volumetric grid element. From each concentration distribution, a spatial distribution of bulk electrical conductivity, σ_b, was derived assuming a linear relation between concentration and σ_b:

$$\sigma_b(\mathbf{x}, t) = \sigma_{b,in} + \beta C(\mathbf{x}, t) \quad (27)$$

where $\sigma_{b,in}$ is the initial background conductivity and β a calibration parameter. In this study, we assumed that $\sigma_{b,in}$ and β are constant in space. $\sigma_{b,in}$ was set to 0.02 S/m and β was chosen to be 5 10^{-6} S m^2 particles^{-1} so that the breakthrough of the solute plume in a plane at 30 m downstream from the injection surface led to a maximum increase in the bulk electrical conductivity by approximately a factor of 10. In reality, $\sigma_{b,in}$ and β vary with location but local values $\sigma_{b,in}$ and β are generally unknown. The impact of this uncertainty on the interpretation of ERT derived σ_b images is briefly discussed in the general discussion and conclusions section.

3.2. Simulation of ERT Data Acquisition

[21] At 30 m downstream from the injection plane ($x_1 =$ 50 m), a fictitious ERT image plane composed of seven boreholes was assumed. The boreholes were set with a separation distance of 10 m between $x_2 = 20$ m and $x_2 =$ 80 m and were each equipped with 26 electrodes between $x_3 = 2.5$ m and $x_3 = 17.5$ m with a vertical separation of 0.6 m. For each electrode, the electric potential field for a current injection at the electrode and a virtual current sink electrode in the middle of the image plane was calculated by solving the Poisson equation:

$$\nabla \cdot \left(\sigma_b(\mathbf{x}, t_j)\nabla\varphi_i(\mathbf{x}, t_j)\right) + I\delta(\mathbf{x} - \mathbf{x}_i) - I\delta(\mathbf{x} - \mathbf{x}_c) = 0 \quad (28)$$

where $\varphi_i(\mathbf{x}, t_j)$ is the electric potential field due to current injection at electrode i at time t_j, δ is the Dirac delta function, $\mathbf{x}_i$ is the position of the electrode i, $\mathbf{x}_c$ the position of the virtual sink electrode (i.e., in the center of the ERT image plane), and I is the current strength at the electrodes. Because of the analogy between the hydraulic head (equation (1)) and the electric potential (equation (28)) equations, equation (28) was solved numerically using the TRACE code. Equation (28) was solved 7644 times (at 42 times for 182 current injection electrodes) using no-flow boundary conditions at the simulation domain boundaries (note that the no-flow boundaries make the use of a virtual sink necessary). For the 2-D inversion, it is assumed that the electrical conductivity field extends infinitely in the x_1 direction. Therefore the length L_1 of the domain for the 3-D

Table 2. Spatial Discretization and Size of Modeling Grids

	Discretization, m			Domain Size, m		
	Δx_1	Δx_2	Δx_3	L_1	L_2	L_3
3-D flow/transport modeling[a]	0.5	0.5	0.1	100	100	20
3-D modeling of electric potential fields[a]	0.5[b]	0.5	0.2	240	70	20
2-D ERT inversion[c]	-	1.0	0.3	-	70	20

[a]Hexaedric elements.
[b]The increment increases with distance from the image plane.
[c]The grid size represents the parameterization used in the 2-D inversion. For the 2.5-D electrical modeling, each rectangular grid cell was divided into four triangular elements.

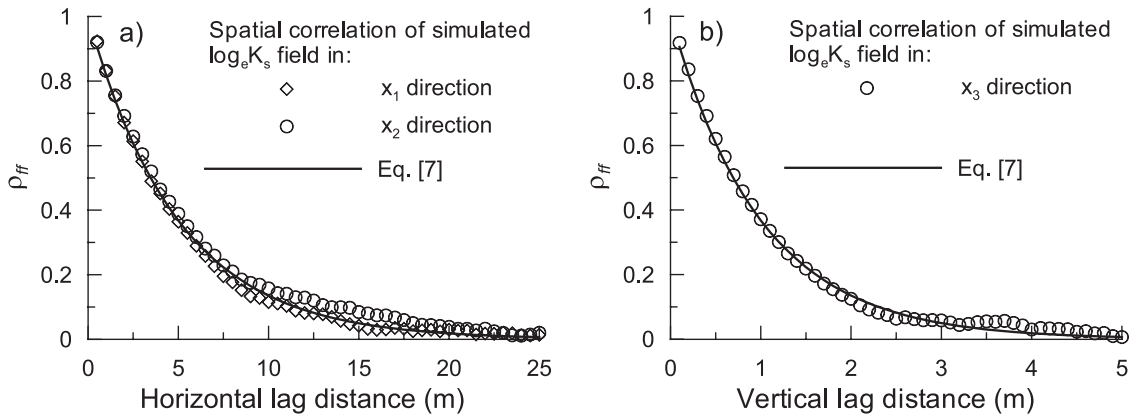

Figure 3. Spatial correlation (ρ_{ff}) of the $\log_e$ transformed hydraulic conductivity (a) in the x_1 and x_2 directions and (b) in the x_3 direction. Solid lines represent the preset spatial correlation function (equation (7)), and the symbols represent the spatial correlation of the generated hydraulic conductivity field.

electric potential field simulation was extended to 240 m (120 m upstream and downstream of the image plane, i.e., from $x_1 = -70$ m to $x_1 = 170$ m) to minimize boundary effects. In order to reduce the numerical load, the grid size was increased in the vertical direction ($\Delta x_3 = 0.2$ m) and the width of the simulation domain was decreased to $L_2 = 70$ m (i.e., from $x_2 = 15$ to $x_2 = 85$ m). In the direction perpendicular to the image plane (x_1) a variable grid size was used: $\Delta x_1 = 0.5$ m between 0 m and 10 m and $\Delta x_1 = 1$ m between 10 m and 20 m from the image plane. The regions between 20 and 120 m from the image plane were discretized using 20 elements in the x_1 direction for each region (upstream and downstream) with a linearly increasing grid size. The electrical conductivities of the larger grid cells were obtained by arithmetic averaging of the conductivities of the smaller cells obtained using equation (27). For the regions between 20 m and 120 m upstream and downstream from the image plane, the conductivity was set equal to the background conductivity.

[22] A transfer resistance data set was assembled according to a "skip-one" dipole-dipole scheme [e.g., *Slater et al.*, 2000] by superposition of the modeled electric potential fields $\varphi_i(t_j)$. The separation distance between electrodes forming a dipole was constant, i.e., 1.2 m. As a consequence, electrodes of an individual dipole are in the same borehole. The electric current was impressed through one dipole and the resulting potential differences were measured using all other dipoles in the same and the neighboring boreholes. For both dipoles in the same borehole, only those potential measuring dipoles were considered which were at least one dipole length (i.e., 1.2 m) from the nearest current electrode to reduce the effect of numerical errors and because the large potential gradients near the current injection dipoles generally exceed the dynamic range of ERT measurement equipment. The transfer resistance at time t_j for a current injection at electrodes i and $i + 2$ and a voltage measurement between electrodes k and $k + 2$, $r_i^k(t_j)$, is calculated from the electric potential fields $\varphi_i(t_j)$ and $\varphi_{i+2}(t_j)$ as

$$r_i^k(t_j) = \frac{\left(\varphi_i(\mathbf{x}_k, t_j) - \varphi_{i+2}(\mathbf{x}_k, t_j)\right) - \left(\varphi_i(\mathbf{x}_{k+2}, t_j) - \varphi_{i+2}(\mathbf{x}_{k+2}, t_j)\right)}{I} \tag{29}$$

where $\mathbf{x}_k$ and $\mathbf{x}_{k+2}$ are the positions of the potential electrodes. Note that because of superposition, the sink term of the virtual electrode in equation (28) cancels out when the difference between $\varphi_i(t_j)$ and $\varphi_{i+2}(t_j)$ is taken so that this difference is independent of the chosen location of the virtual electrode, $\mathbf{x_c}$. The dipole polarity was chosen such as $r_i > 0$. Only those "measurements" where r exceeds 5.10^{-4} Ω were retained in order to simulate a minimum voltage that can be reliably determined by typical ERT instruments, here e.g., 0.5 mV for a current of 1 A. This resulted in approximately 4500 transfer resistance measurements in each data set for a particular time t_j.

[23] For each time t_j, a noise contaminated data vector of $\log_e$ transformed resistances, $\mathbf{d}$, was constructed:

$$d_i = \log_e(r_i) + \varepsilon_i \tag{30}$$

where ε_i is a zero-mean uncorrelated Gaussian random noise with a standard deviation of 0.02 (corresponding to 2% of r_i). Note that the $\log_e$ transform is used because of the typically large dynamic range of transfer resistances in ERT data sets.

3.3. Two-Dimensional Tomographic Inversion of ERT Data Sets

[24] In ERT, the spatial distribution of bulk electrical conductivity, σ_b, is reconstructed from a data set of transfer resistance measurements. This involves the discretization of the σ_b distribution in a finite element or finite difference grid, forward modeling of the data set for a given σ_b distribution, and the minimization of an objective function. Following the approach of *Daily et al.* [1992] and *LaBrecque et al.* [1996], the following objective function Ψ is used:

$$\Psi(\mathbf{m}) = \| \mathbf{W}(\mathbf{d} - \mathbf{f}(\mathbf{m})) \|^2 + \alpha \| \mathbf{Rm} \|^2 \tag{31}$$

where $\mathbf{m}$ is the parameter vector with $\log_e$ transformed σ_b of the finite element (difference) grid, $\mathbf{f}$ is the operator of the forward model, $\mathbf{W}$ is a diagonal matrix containing data weights, $\mathbf{R}$ is a matrix evaluating the roughness of the $\log_e\sigma_b$ distribution (here, $\|\mathbf{Rm}\|^2$ is the discrete approximation of $\int\int \|\nabla \log_e \sigma_b\|^2 \, dx_2 dx_3$), and α is a regularization parameter which balances data misfit and model roughness

in the objective function. For cross-borehole electrode arrangements in a 2-D plane an ERT data set predominantly contains information about the electrical conductivity distribution in this plane, while, in comparison, information content on off-plane conductivity variations is strongly limited due to the spatially biased sensitivity characteristics of individual cross-borehole ERT measurements [e.g., *Spitzer*, 1998]. Therefore, for the inversion of ERT data associated with coplanar cross-borehole electrode arrangements, the electrical conductivity distribution is commonly considered as a 2-D distribution in the considered plane (image plane), which is constant in the perpendicular (x_1) direction. The forward model **f**, i.e., the 3-D Poisson equation (28), then simplifies to a 2-D problem after performing a 1-D Fourier cosine transform with respect to the x_1 direction, which is assumed to be of infinite extent [e.g., *Kemna*, 2000]. In practice, mixed boundary conditions are generally used at the lateral and bottom boundaries within the half-space to account for partial current flow across the boundary [e.g., *Dey and Morrison*, 1979]. However, in order to be consistent with the ERT data acquisition simulation, we here imposed no-flow boundary conditions at all boundaries. The effect of the type of boundary condition on the quality of the inverted ERT images is minimal, provided that both forward model (or data) and inverse model satisfy the same condition. This was analyzed by inverting simulated data for a 2-D σ_b distribution using a no-flow boundary condition at the top boundary (Earth's surface) and, respectively, mixed and no-flow boundary conditions at the lateral and bottom boundaries, and comparing the corresponding imaging results. Since the iterative minimization of equation (31) involves numerous runs of the forward model **f** for different parameter fields **m**, the spatial resolution of the parameter field was reduced: Δx_2 was increased to 1 m and Δx_3 to 0.3 m. A summary of the grid sizes used for the flow and transport simulation, the simulation of the 3-D electric potential fields used for the generation of the ERT data set, and the parameterization used for the 2-D inversion of the ERT data sets is given in Table 1.

[25] The data are weighted by a weighting factor, W_{ii}, which is inverse proportional to the data error. The initial data weights are represented by the following error model [e.g., *LaBrecque et al.*, 1996]:

$$W_{ii} = \left(a + \frac{b}{r_i}\right)^{-1} \tag{32}$$

In accordance with the noise model equation (30), the parameter a, which represents the relative resistance error, was chosen to be 0.02. The parameter b was set to 10^{-5} Ω and represents an absolute error of the modeled resistances corresponding to the maximum numerical accuracy. The chosen relative noise level of 0.02 and absolute error of 10^{-5} Ω are relatively low. In practice, not only uncertainty in the measurements, but also systematic errors associated with the modeling and measurement approaches (e.g., borehole effects, 2-D representation of a 3-D σ_b distribution) must be accounted for, so that an error level of more than 0.1 is not uncommon for cross-hole ERT [e.g., *Kemna*, 2000]. However, for monitoring purposes, the temporal changes in electrical conductivities are of interest. In the so-called "difference" inversion approach [*LaBrecque and Yang*, 2001], any static sources of errors are cancelled out by subtracting an initial or reference data set $\mathbf{d}_0$ and modeling result $\mathbf{f}(\mathbf{m_0})$ from the data set **d** and modeling result **f**(**m**), respectively, at a later time. As a consequence, the chosen error model parameters were found to be realistic for ERT difference inversion (e.g., *Kemna et al.* [2002] used a 0.03 relative noise level). In our synthetic study, the initial σ_b distribution is homogeneous and static measurement errors are not considered so that a difference inversion would yield exactly the same result as an "absolute" inversion. The data weighting matrix was updated after each inverse iteration step using the "robust" data reweighting algorithm proposed by *LaBrecque and Ward* [1990]. This procedure reduces the weight of individual data with a large misfit and has been shown to be effective for the processing of noisy data [e.g., *Morelli and LaBrecque*, 1996]. A Gauss-Newton scheme was used for the iterative minimization of the objective function, equation (31). At each iteration step, a univariate search was preformed to find the optimum value of α. The iteration was stopped when the root-mean square measure of the data misfit in equation (31) reached 1 for the largest possible value of α. Further details on the used forward modeling and inversion algorithms are given by *Kemna* [2000].

3.4. Derivation of Equivalent Parameters From Simulated and Inverted Breakthrough Curves

[26] Equivalent transport parameters were determined on 7 reference planes at 10 m to 70 m from the initial position of the tracer. Time series of concentration images that were inverted from the ERT data sets at 30 m from the injection plane were analyzed in the same way.

[27] The stream tube model parameters λ_s and v_s were calculated for each pixel with $T_0 > 20000$ #Particles d m^{-3} where T_0 is the zeroth moment of the BTC which is defined as

$$T_0(\mathbf{x}) = \int_0^\infty C(\mathbf{x}, t)dt \tag{33}$$

[28] For each pixel, T_0 was calculated using a numerical integration of the concentration breakthrough. Before integrating an ERT inverted BTC, all concentration values smaller than 20 #Particles m^{-3} were set to 0. For the simulated BTCs, the method of moments was used to determine the STM parameters whereas for the inverted BTCs, the STM parameters were obtained from fitting the solution of the 1-D CDE to the local BTC (equation (18)). Parameters were fitted because negative concentrations (i.e., bulk electrical conductivities smaller than the background) were occasionally observed in the inverted concentration images due to inversion artifacts. Since time moments are strongly influenced by concentrations in the tail of the breakthrough, especially the higher moments, negative concentrations in the tailing part of the breakthrough occasionally led to artificially small mean arrival times and negative travel time variance.

[29] To calculate the spatially averaged solute flux concentration $\langle C^f(x_1, t)\rangle$, local solute fluxes must be derived by multiplying the local concentrations with the local water flux (equation (9)) across the reference plane. However, with current measurement techniques, it is

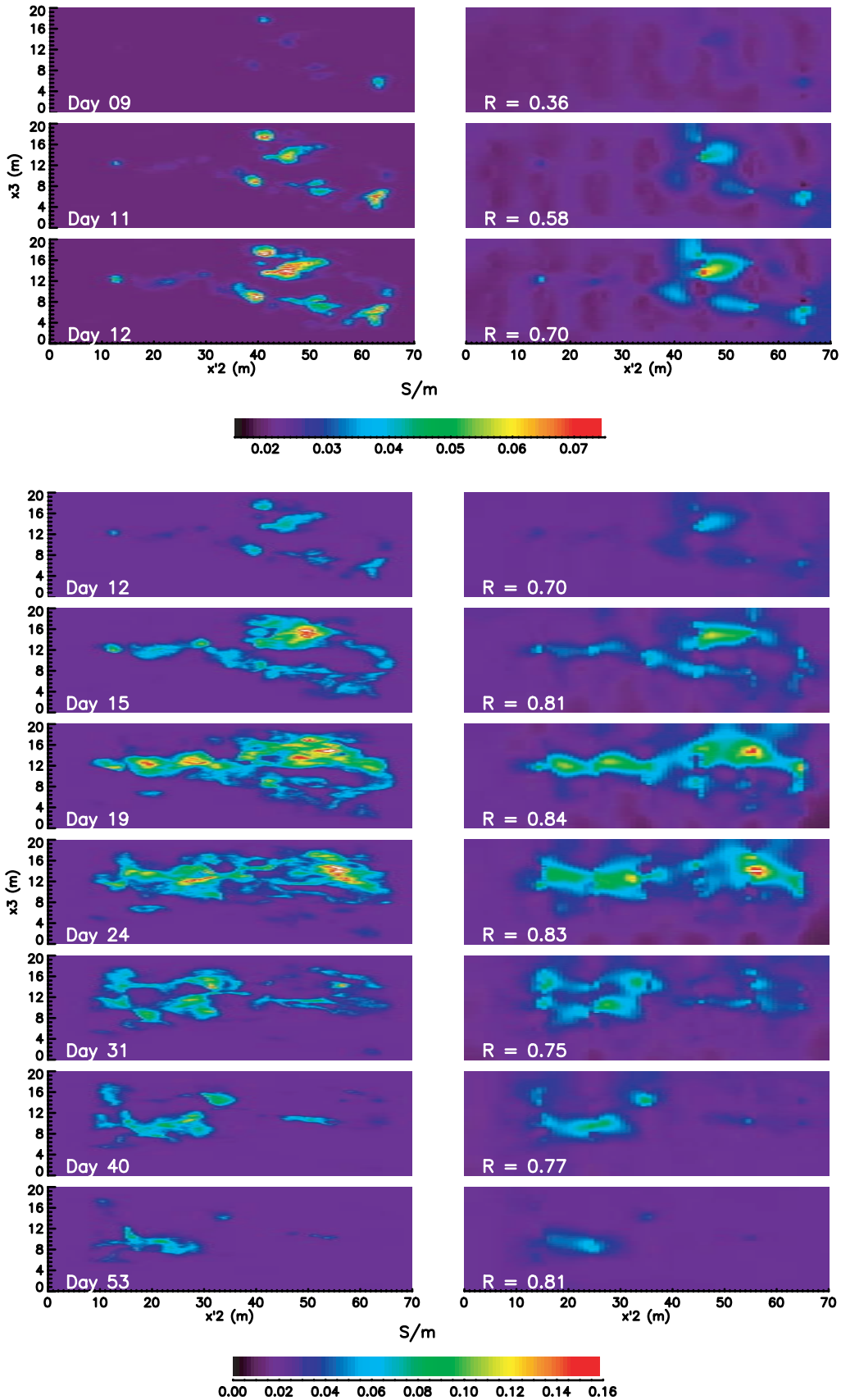

Figure 4. (left) Simulated and (right) ERT inverted electrical conductivity distributions in the ERT image plane at different days after injection of the tracer plume. R is the pixel-wise correlation coefficient between simulated and inverted electrical conductivities. (Note the different color scale used for the top six plots.)

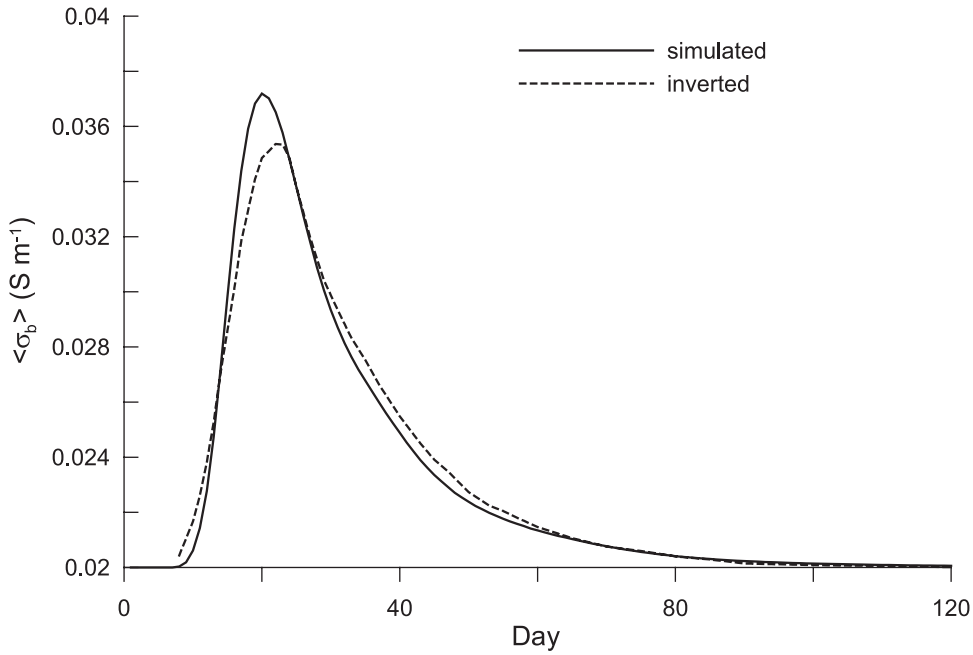

Figure 5. Breakthrough curve of the spatially averaged bulk electrical conductivity, $\langle\sigma_b\rangle$, in the ERT image plane. Solid line represents simulated $\langle\sigma_b\rangle$, and dashed line represents the ERT inverted $\langle\sigma_b\rangle$.

impossible to determine images of local water fluxes so that average solute fluxes must be approximated on the basis of concentration images. *Vanderborght and Vereecken* [2001] discussed different approaches to approximate flux averaged concentrations in a reference plane based on local concentration measurements. In a first approximation, it is assumed that local water fluxes and solute concentrations are not correlated ($\langle q_1(\mathbf{x})\ C(\mathbf{x},\ t)\rangle = \langle q_1(\mathbf{x})\rangle\ \langle C(\boldsymbol{x},\ t)\rangle$) so that the flux averaged concentration is approximated by the volume averaged concentration ($\langle C^f(x_1,\ t)\rangle \approx \langle C^r(x_1,\ t)\rangle$). When the particle arrival time at a certain location on the reference plane is inversely correlated with the local water flux at this location, this approximation underestimates the average solute flux concentrations in the early stage of the breakthrough and overestimates them in the later stage. In a second approximation, it is assumed that the local water fluxes are correlated with the stream tube velocities so that from equation (9) follows that the flux averaged concentrations are approximated by the velocity weighted local concentrations:

$$\langle C^f(x_1,t)\rangle \approx \frac{\langle v_s(\mathbf{x})C^r(\mathbf{x},t)\rangle}{\langle v_s(\mathbf{x})\rangle} \tag{34}$$

The average BTCs were calculated using pixel values of simulated and inverted bulk electrical conductivities in the region 2 m $< x_3 <$ 18 m and 15 m $< x_2 <$ 85 m (or 0 m $< x_2' <$ 70 m).

4. Results and Discussion

4.1. Direct Comparison Between Simulated and ERT Inverted σ_b Images

[30] Images of simulated and ERT inverted electrical conductivities, σ_b, in the ERT reference plane are shown for different days after solute injection in Figure 4. Looking at the spatially averaged σ_b in the reference plane, $\langle\sigma_b\rangle$ (Figure 5), the ERT inverted images reproduce the arrival and the magnitude of the mean solute peak fairly well. The magnitude of the mean solute peak or the overall contrast in the ERT inverted images when the peak breaks through (days 19 and 24 in Figure 4) is somewhat smaller. The rising and falling limbs of the $\langle\sigma_b\rangle$ BTC are relatively well reproduced as well. However, the ERT derived $\langle\sigma_b\rangle$ BTC shows an earlier breakthrough and higher values in the tailing part until approximately 80 days after solute injection. From day 8 until day 12, ERT derived $\langle\sigma_b\rangle$ are clearly larger than the simulated $\langle\sigma_b\rangle$. The contrast in the ERT σ_b images is smaller than in the simulated images (Figure 4). Also the ERT inverted images in the tailing part (e.g., day 40 and day 53) exhibit a smaller contrast despite a higher $\langle\sigma_b\rangle$.

[31] The larger-scale structures of the simulated σ_b images are well preserved in the ERT inverted σ_b images. The anisotropy of the hydraulic conductivity field with a larger spatial correlation in the horizontal than in the vertical direction is clearly reflected in the structure of the simulated tracer distributions. Despite an isotropic smoothing, which was imposed as regularization, the ERT inverted σ_b images reproduce the anisotropic character of the simulated σ_b distributions. The smoothing operator, the lower spatial resolution of the ERT parameterization, as well as the diffusive nature of electric field itself lead to a reduced spatial resolution of the inverted σ_b images. Small-scale structures are smeared out reducing local conductivity peaks. Considering a pixel-wise correlation coefficient between simulated and inverted σ_b images (to calculate the pixel-wise correlation, the larger pixels of the inverted σ_b images were divided into 6 pixels of the same size as in the simulated images; see Table 2) (Figure 4), the

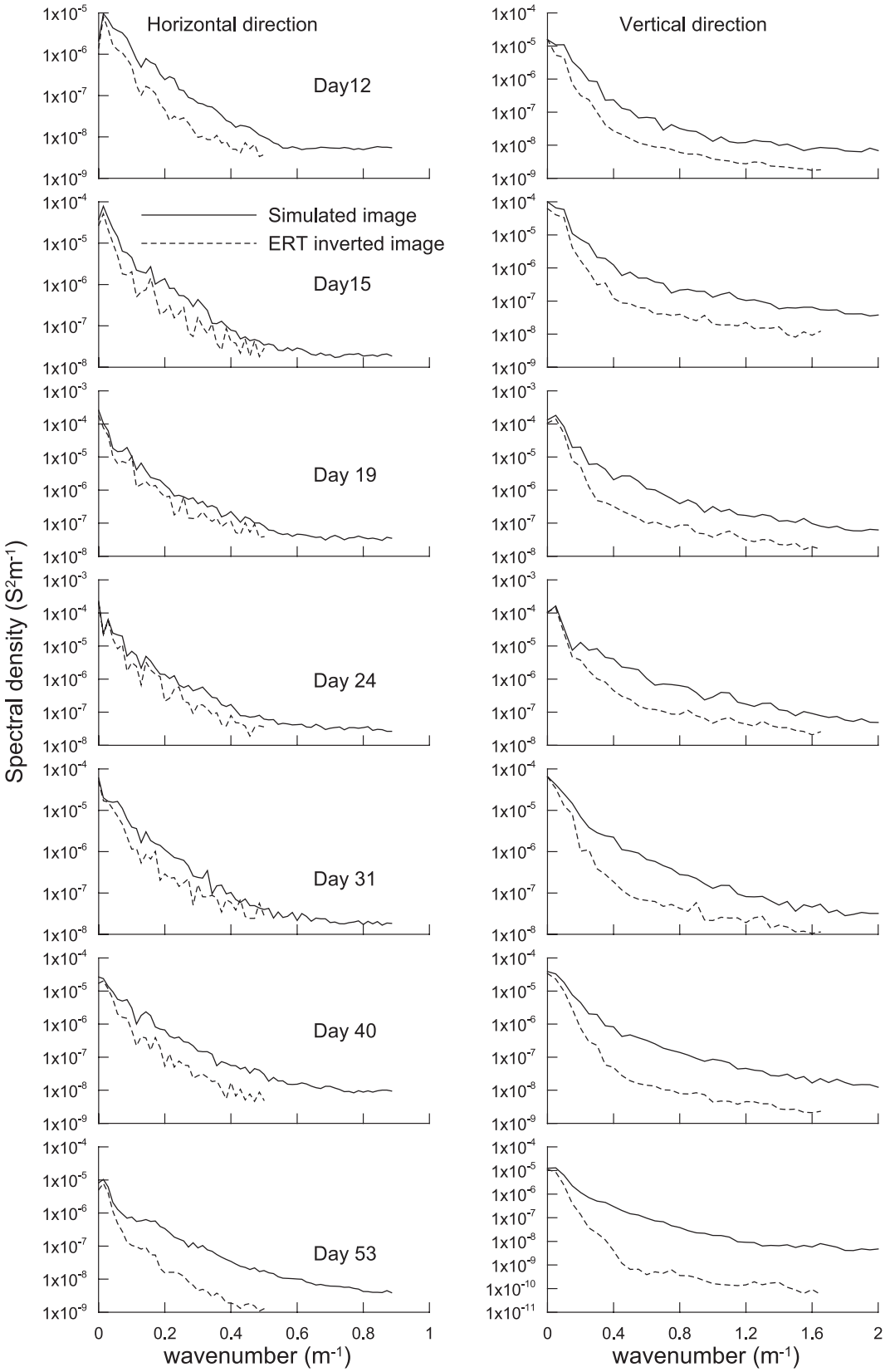

Figure 6. Spectral densities in the (left) horizontal and (right) vertical directions of the simulated (solid lines) and ERT inverted (dashed lines) σ_b images.

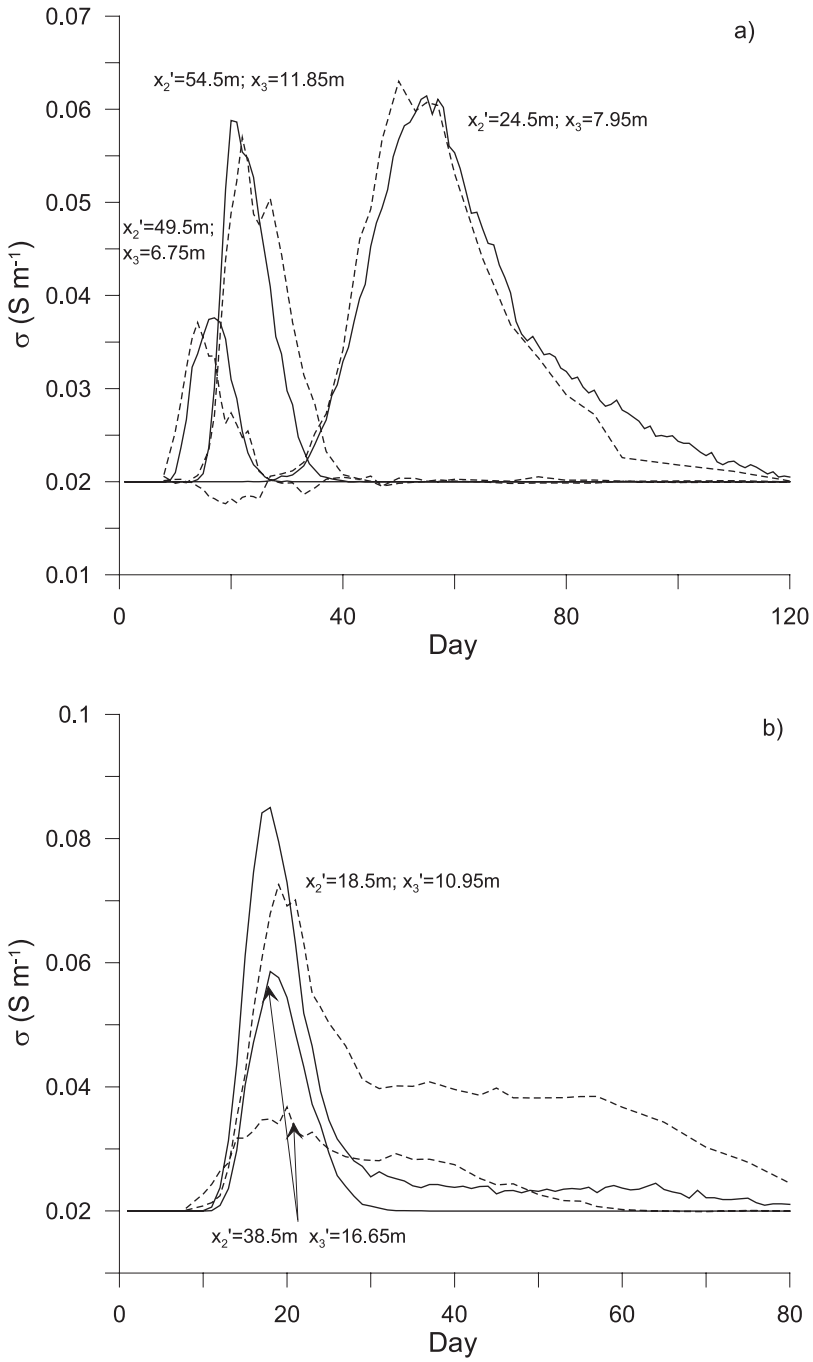

Figure 7. Examples of local breakthrough curves in terms of bulk electrical conductivity (a) at locations where simulated (solid lines) and ERT inverted (dashed lines) curves match fairly well and (b) at locations where the agreement is less good.

correlation is highest when the solute peak breaks through (day 19 and day 24) whereas it decreases when the solute mass or the overall contrast in the image is lower. The spatial resolution of the simulated and inverted σ_b images is quantified by the wave number spectra of the images, which are shown in Figure 6. Since the structures in the σ_b images are of larger extent in the horizontal than in the vertical direction, the horizontal spectra drop off faster with increasing wave number than the vertical ones. The effect of smoothing is clearly reflected in the spectra of the ERT inverted images showing a loss of information, i.e., a lower spectral density at higher frequencies. The loss of spectral information is more significant in the vertical than in the horizontal direction. Also important to note is that the loss of high-frequency information is larger at the beginning (day 12) and end (day 40, day 53) of the plume breakthrough.

[32] The decrease in pixel correlation and the loss of high-frequency information at the beginning and end of the solute breakthrough can be explained by the lower signal of the tracer plume, the smoothness constraint, and the 2-D approximation of the 3-D conductivity distribution. In the

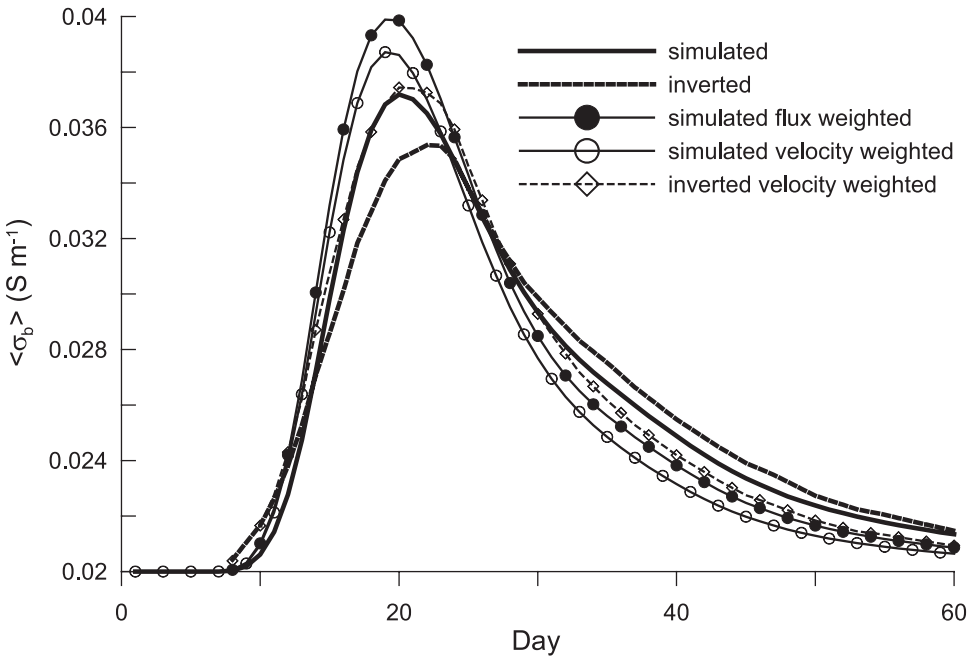

Figure 8. Breakthrough curves of averaged bulk electrical conductivities, $\langle\sigma_b\rangle$, in the ERT image plane obtained from transport simulations (solid lines) and from inverted ERT data sets (dashed lines). Spatial averages (thick lines), flux weighted averages (solid circles), and stream tube velocity weighted averages (open circles and diamonds) (equation (34)) are shown.

ERT inversion, the roughness of the model, which is related to the model contrast, is minimized subject to fitting the data to an acceptable degree (noise level). For a decreasing model contrast, the signal-to-noise ratio decreases. As a consequence, the smoothness constraint leads to a more pronounced decrease in spatial resolution and contrast in the inverted image when the model contrast decreases. This illustrates the relevance of the signal-to-noise ratio and the error model (equation (32)) for the quality of the inverted images.

[33] The 3-D electric current distribution is influenced by the electrical conductivity distribution upstream and downstream from the ERT image plane. As a consequence, the transfer resistances are affected by the conductive solute plume when it has not yet reached (rising limb of the $\langle\sigma_b\rangle$ BTC) and already left (falling limb) the image plane. However, this effect does not result in the appearance of clearly delineated artificial features in the inverted images but is of a more diffuse character.

[34] Both the pixel correlation and the wave number spectra are integrative measures of the correspondence between the simulated and inverted σ_b images. In Figure 7 the simulated and ERT inverted BTCs in a few selected pixels are shown. Simulated local BTCs were averaged over neighboring pixels to achieve the same averaging area or pixel size as in the ERT inverted images. At some locations the simulated and inverted BTCs agree fairly well (Figure 7a) whereas the agreement is not good at other locations (Figure 7b). The arrival of the concentration peak is well reproduced but the spreading is largely overestimated at some locations. These locations correspond with locations where the variability in peak arrival times in neighboring pixels is large (see next section). The large deviation at some locations between simulated and ERT inverted pixel-scale BTCs illustrates that large deviations between σ_b values derived from local-scale groundwater sampling and from ERT images are not unexpected.

4.2. Interpretation of Local and Averaged BTCs Using Equivalent Transport Models

[35] The effect of the averaging procedure on the estimation of large-scale averaged breakthrough curves in a reference plane is illustrated in Figure 8. Since we assumed a spatially constant relation between σ_b and C (equation (27)), the spatially averaged σ_b correspond with $\langle C^r(x_1, t)\rangle$ whereas the flux and velocity weighted σ_b represent $\langle C^f(x_1, t)\rangle$ and its approximation through equation (34), respectively. The flux averaged σ_b BTC shows a larger peak concentration and earlier peak breakthrough than the nonweighted σ_b BTC. Using stream tube velocities as a proxy for the local water flux, a relatively good approximation of the flux weighted BTC is obtained. However, the velocity weighted average σ_b are smaller than the flux weighted averages. This is explained by the exclusion in the velocity weighted average of pixels at fringes of the plume where the local tracer signal was too small (i.e., $T_0 < 20000$) to calculate the stream tube velocity. However, differences between averaged BTCs using different averaging weights are of the same order of magnitude as those between averaged BTCs calculated from simulated and inverted σ_b distributions.

[36] The equivalent dispersivity, λ_{eq} (equation (14)), derived from averaged concentrations in the reference plane is plotted against the travel distance in Figure 9. The first-order prediction of λ_{eq} (equation (21)) at different distances from the injection plane is relatively well in agreement with λ_{eq} derived from the numerical simulations, which is in line with previous studies of transport in generated heteroge-

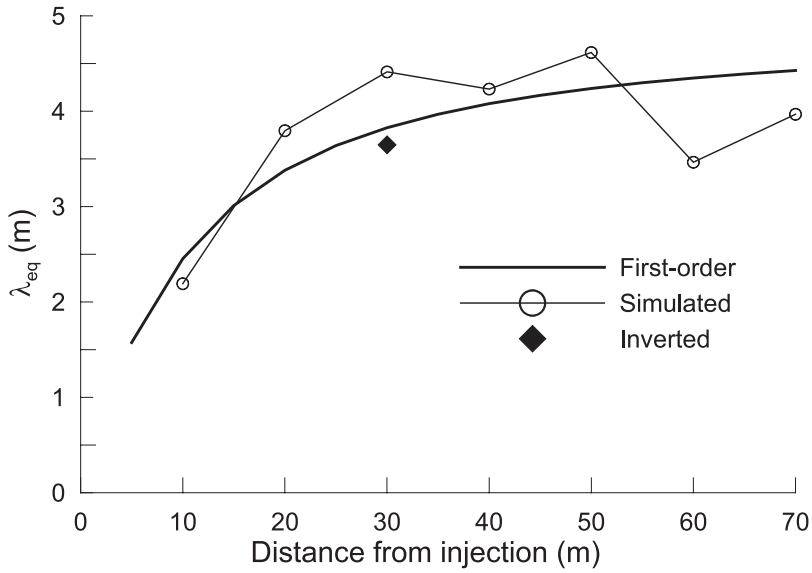

Figure 9. Equivalent dispersivity, λ_{eq}, derived from temporal moments of spatially averaged breakthrough curves (equation (14)) of simulated and ERT inverted concentrations in reference planes at different distances from the injection plane and λ_{eq} predicted from first-order theory (equation (21)).

neous media with $\sigma_f^2 = 1$ [e.g., *Bellin et al.*, 1992]. The λ_{eq} derived from the inverted ERT data sets is somewhat smaller than λ_{eq} from the simulated concentrations. This seems at first sight contradictory to the BTC of the averaged inverted concentrations (Figure 8) which has a lower peak concentration and a larger spreading than the BTC of the simulated averaged concentrations. However, in the tailing part of the BTCs (after day 80) the inverted average concentrations are smaller than the simulated ones (Figure 5). Since concentrations in the tailing part have a large impact on the second temporal moment, λ_{eq} turns out to be larger for the simulated than for the inverted average BTC.

[37] The distribution of the STM parameters that were derived from the simulated and inverted local BTCs are shown in Figure 10. Figures 10a and 10b show the distribution of the time integrated concentration. The range of simulated and inverted T_0 is similar and the overall spatial pattern of the simulated T_0 is well recovered in the inverted T_0 image. However, the inverted T_0 image appears to be more blurred and local high T_0, which appear in thin horizontal bands, are smoothed out. This is an obvious consequence of the isotropic smoothness constraint that was applied in the inversion of the ERT data sets. For the stream tube velocity distributions, v_s (Figures 10c and 10d), basically the same conclusions as for the T_0 images can be drawn. The simulated v_s image shows less small-scale variations than the simulated T_0 image and the larger anisotropic structures in the simulated v_s image are better recovered in the inverted image. The agreement between the simulated and inverted stream tube dispersivity, λ_s, images (Figures 10e and 10f) is clearly less good with the average simulated λ_s being considerably smaller than the average inverted λ_s. The location of the vertical electrode chains is clearly visible in the image of inverted λ_s. The lower inverted λ_s values close to the electrode chains are in better agreement with the simulated λ_s values. This effect may be explained by a decrease of spatial resolution of the inverted concentration images with increasing distance from the electrode chains. Because of a lower spatial resolution, the breakthrough in neighboring pixels is integrated which leads to a higher apparent λ_s, especially when the stream tube velocity, v_s, is different in the "joined" pixels. A closer inspection of the λ_s and v_s images reveals that the inverted λ_s overestimate the simulated λ_s especially in those regions where the gradient of v_s is large. A comparison between simulated, inverted, and first-order predicted λ_s is shown in Figure 11. Since the simulated and first-order predicted λ_s match fairly well, a fit of the first-order prediction model to λ_s derived from measurements may be used to infer, for instance, the local-scale dispersion coefficient from locally measured BTCs as was done by *Vanderborght and Vereecken* [2002]. Using the inverted λ_s value averaged over the entire image would lead to an overestimation of the local-scale dispersion. If only the inverted λ_s in the pixels in the proximity of electrode chains (less than 1m distance from the electrode chain) are considered, the average simulated λ_s is better approximated.

[38] The spatial correlation of the simulated and inverted v_s, $\rho_{v_s v_s}(\mathbf{h}) = C_{v_s v_s}(\mathbf{h})/C_{v_s v_s}(\mathbf{0})$, and its first-order prediction are shown in Figure 12. For the horizontal direction, the inverted and simulated $\rho_{v_s v_s}(\mathbf{h})$ are in close agreement. Although the shape of the simulated/inverted $\rho_{v_s v_s}(\mathbf{h})$ is somewhat different from the shape of the first-order approximation, the overall agreement is good. The deviations between simulated and first-order predicted $\rho_{v_s v_s}(\mathbf{h})$ can be explained by the fact that only one realization of the transport process of a limited spatial lateral extent is considered. Using more realizations or considering a larger lateral extent of the solute plume are expected to reduce these deviations.

[39] In the vertical direction, the inverted $\rho_{v_s v_s}(\mathbf{h})$ shows a somewhat larger spatial correlation than the simulated $\rho_{v_s v_s}(\mathbf{h})$. This is a result of the smoothing in the inversion of the ERT data sets in combination with the smaller spatial correlation of v_s in the vertical direction due to the

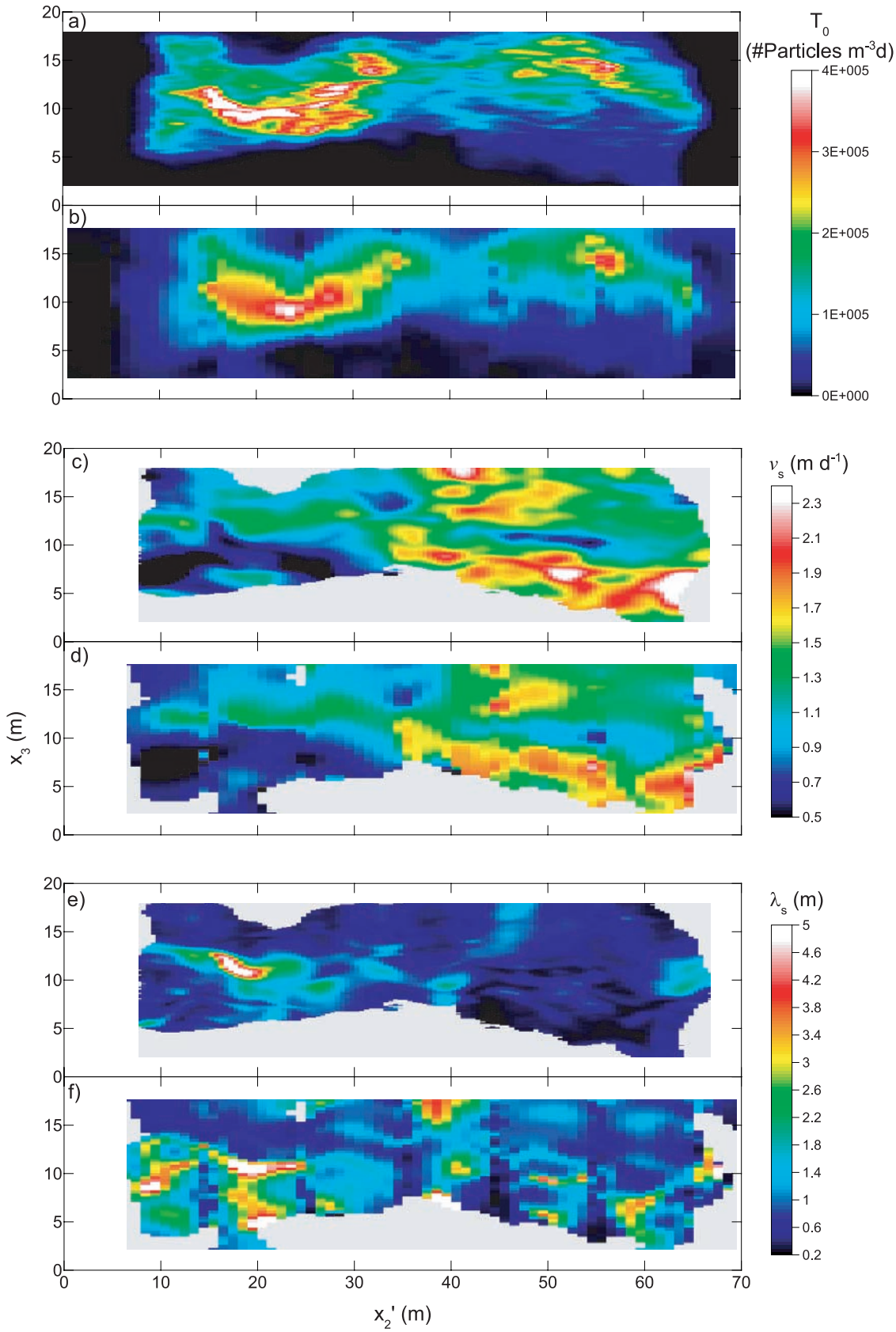

Figure 10. Spatial distribution of parameters derived from simulated (Figures 10a, 10c, and 10e) and ERT (Figures 10b, 10d, and 10f) inverted local breakthrough curves in the ERT image plane: (a and b) zeroth moment of the BTCs T_0 (equation (33)), (c and d) stream tube velocity v_s (equation (13)), and (e and f) stream tube dispersivity, λ_s (equation (15)).

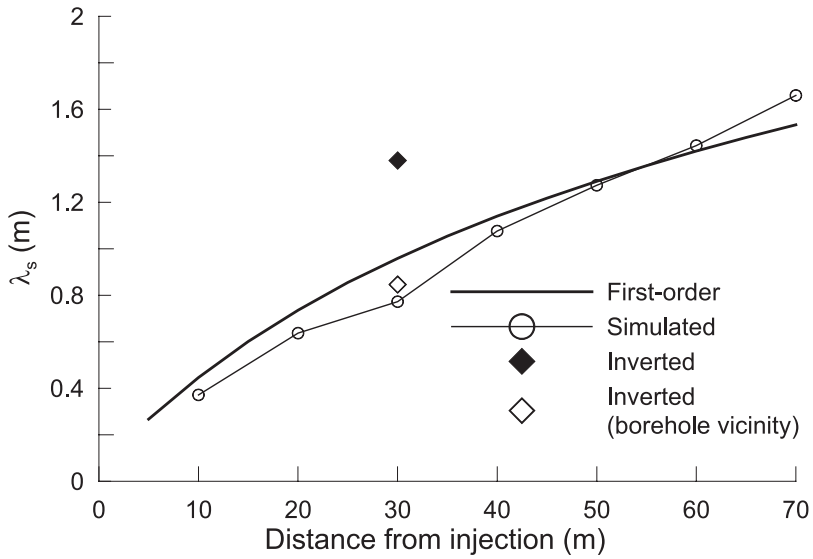

Figure 11. Spatial average of the stream tube dispersivity, λ_s, derived from simulated local BTCs in reference planes at different distances from the injection plane (circles), from ERT inverted local BTCs (solid diamond, spatial average over the image plane; open diamond, average only in the pixels adjacent to the ERT electrode chains), and from first-order prediction (solid line) (equation (24)).

anisotropy of the hydraulic conductivity field. The first-order approximation predicts a smaller spatial correlation in the vertical direction than the simulated v_s. This deviation may be again the result of the limited lateral extent of the tracer plume.

[40] The spatial correlation of v_s is determined by the spatial correlation of the hydraulic conductivity. The travel distance or travel time and the local-scale dispersion, $\mathbf{D_d}$, are also expected to have an impact on $\rho_{v_s v_s}$ (**h**). The calculation of $\rho_{v_s v_s}$ (**h**) involves the integration of the spatial correlation of the pore water velocities, $\rho_{u_1 u_1}$ (**h**), along the travel paths of two different particles, of which the deviation from the mean particle trajectory is determined by the local-scale dispersion (see equation (26)). In Figure 13 the effect of $\mathbf{D_d}$ (expressed in terms of the dimensionless Peclet number: $Pe = \gamma_1/\lambda_{dL}$) and travel distance on $\rho_{v_s v_s}$ (**h**) is shown. Because of local-scale dispersion, local concentration differences are smoothed out progressively with time, so that the spatial correlation of v_s is expected to increase with time and $\mathbf{D_d}$. The first-order predictions show, however, that $\rho_{v_s v_s}$ (**h**) increases only weakly with increasing travel time/distance and local-scale dispersion. The simulated $\rho_{v_s v_s}$ (**h**) even decrease with travel distance.

[41] Since $\rho_{v_s v_s}$ (**h**) is little influenced by $\mathbf{D_d}$ and travel time/distance, the spatial correlation scale, γ_i, of the hydraulic conductivity could be derived from the measured $\rho_{v_s v_s}$ (**h**) by a first-order prediction model fit using a rough estimate of $\mathbf{D_d}$. As shown above, ERT offers the possibility to derive $\rho_{v_s v_s}$ (**h**) with sufficient spatial resolution so that the spatial correlation of $\log_e K_s$ may be derived indirectly from a tracer experiment. Since λ_{eq} is only little influenced by $\mathbf{D_d}$ [*Fiori*, 1996] the variance of the $\log_e$ transformed K_s may be derived in a second step using the spatial correlation of K_s which was derived from $\rho_{v_s v_s}$ (**h**). In a last step, the local-scale dispersion, $\mathbf{D_d}$, may be derived from λ_s when the variance and spatial correlation of K_s are known. This procedure can be repeated using the updated $\mathbf{D_d}$, σ_f^2, and γ_i until the estimates have converged.

5. General Discussion and Conclusions

[42] We illustrated by means of a synthetic experiment that tracer movement across a reference plane in a heterogeneous aquifer can be characterized in a quantitative way using a combination of ERT, equivalent transport models, and first-order approximations of the stochastic flow and transport equations. General features of the spatiotemporal tracer breakthrough pattern in the reference plane were well recovered in the ERT inverted images but clearly influenced by the smoothness constraint and the 2-D representation of the 3-D electrical conductivity distribution, which are imposed in the data inversion process. Importantly, the effects of the smoothness constraint are clearly dependent on the data error level and model contrast. For a lower model contrast and a corresponding smaller signal-to-noise ratio, the spatial resolution and the contrast in the ERT inverted images are more reduced.

[43] Despite the relatively good overall agreement between the simulated and ERT inverted images, local-scale electrical conductivities may deviate considerably, especially in regions where larger gradients in solute peak arrival time exist. As a consequence, a calibration or a validation of ERT derived σ_b images on the basis of local-scale groundwater monitoring may be difficult.

[44] The spatiotemporal information that is gained about the transport process was interpreted using equivalent 1-D convection dispersion models. Using first-order approximate solutions of the stochastic flow and transport equations, the equivalent parameters of these models were linked to the local-scale dispersion tensor and to the statistical parameters which characterize the spatial heterogeneity of hydraulic conductivity. Equivalent parameters and their spatial correlation which were derived from the transport

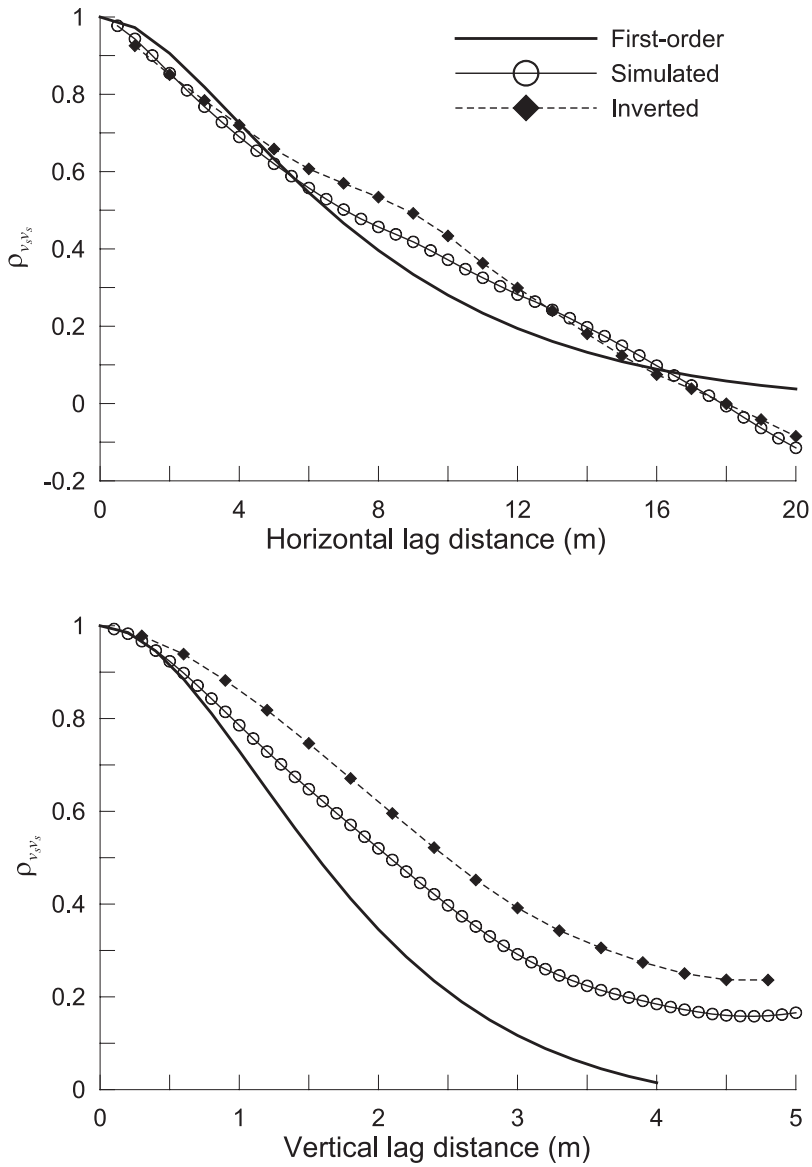

Figure 12. Spatial correlation of the stream tube velocities, $\rho_{v_s v_s}$ (**h**), in the ERT image plane in the (top) horizontal and (bottom) vertical direction derived from simulated local BTCs (circles), ERT inverted BTCs (diamonds), and first-order predicted $\rho_{v_s v_s}$ (**h**) (solid line) (equations (25) and (26)).

simulation and the first-order solutions were, for the considered heterogeneity $\sigma_f^2 = 1$, similar. This validates the used first-order approximate solutions of the stochastic flow and transport equations, which may therefore be used to derive the local-scale dispersion and the geostatistical parameters of the hydraulic conductivity in an inverse way. This allows the characterization of the subsurface heterogeneity in an indirect way by monitoring of the transport process.

[45] Since $\rho_{v_s v_s}$ (**h**) is relatively insensitive to local-scale dispersion and travel distance, it is an important source of information about the structure of the hydraulic conductivity field and can be used to infer its spatial correlation. A major problem with conventional borehole observations is the lack of spatial resolution to derive $\rho_{v_s v_s}$ (**h**) in the horizontal direction. In this study, the highest spatial resolution that could be obtained using borehole information was 10 m. This would be clearly insufficient to capture the spatial correlation of v_s in the horizontal direction since $\rho_{v_s v_s}$ (**h**) could be determined only for $h_2 = 0$ m, 10 m, and 20 m (Figure 12). Using ERT, the spatial pattern of local stream tube velocities between two observation wells could be resolved and the spatial resolution with which $\rho_{v_s v_s}$ (**h**) could be determined in the horizontal direction was about an order of magnitude higher than the distance between the boreholes. Therefore ERT offers the possibility to determine $\rho_{v_s v_s}$ (**h**), from which the correlation scale of the hydraulic conductivity in the horizontal direction, which is a key parameter for transport in a heterogeneous aquifer but is difficult to determine using classical techniques, could be inverted. Because of a loss of spatial resolution in the ERT images, the mixing or dilution of the local-scale tracer concentrations, which is quantified by the stream tube dispersivity, λ_s, was overestimated, especially in regions in the middle between the boreholes and at locations with large

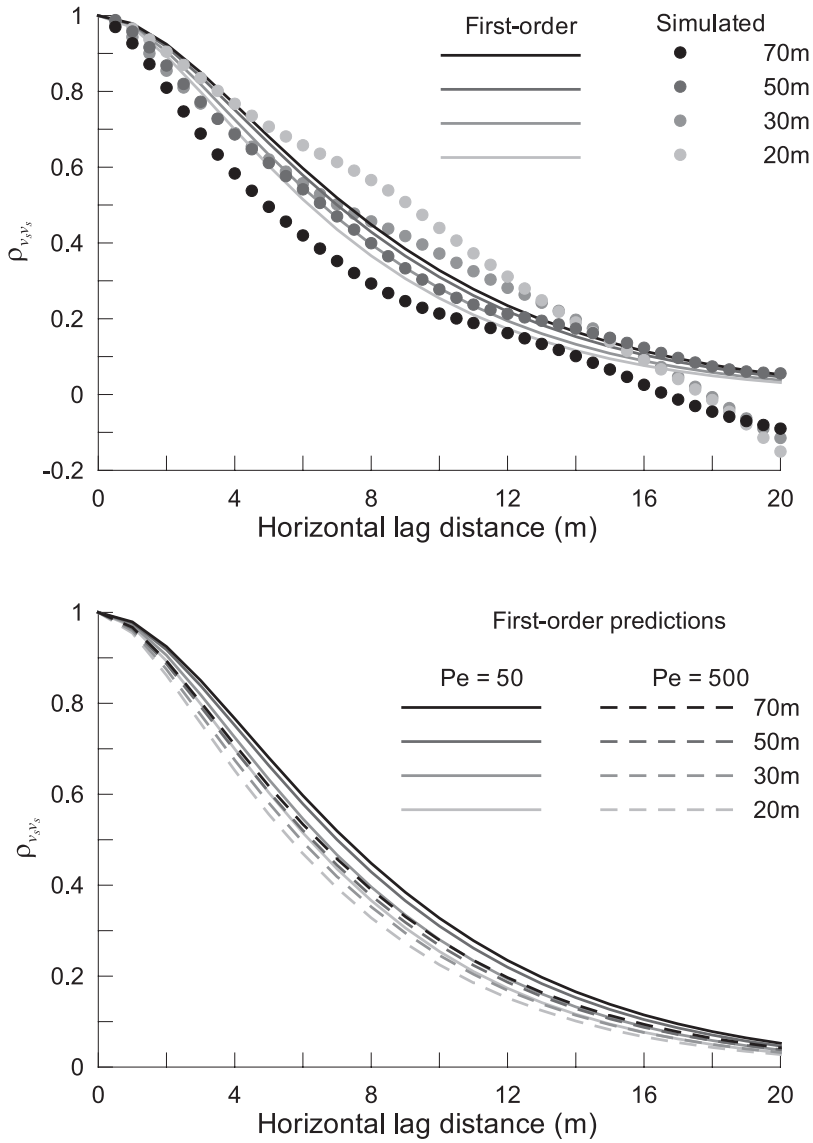

Figure 13. Effect of travel distance and local-scale dispersion on spatial correlation of the stream tube velocities. (top) First-order predictions of $\rho_{v_s v_s}$ (**h**) and $\rho_{v_s v_s}$ (**h**) derived from simulated local BTCs in reference planes at different distances from the injection plane. (bottom) First-order predictions of $\rho_{v_s v_s}$ (**h**) at different distances from the injection plane for two different Peclet numbers: $Pe = \gamma_1/\lambda_L$.

local gradients in stream tube velocity. Closer to the boreholes, where the ERT resolution is higher, λ_s estimated from ERT images was close to the simulated λ_s.

[46] These results illustrate that despite the assumptions that are made in the inversion of the ERT data sets (smoothness constraint, assumption of a 2-D distribution of the bulk electrical conductivity) the method can be used for a quantitative characterization of the subsurface transport process. However, the ERT inverted equivalent transport parameters and the spatial resolution of the ERT images depend on the model contrast, error noise, and electrode configuration. Understanding the effect of these factors on the ERT inversion results requires further systematic investigations. The ERT inverted equivalent transport parameters may be used as evaluation criteria in such studies.

[47] Although we designed the synthetic experiment to be close to realistic conditions (with respect to the electrode arrangement, noise level in the acquired ERT data sets, background electrical conductivity and conductivity contrast generated by the salt tracer plume, heterogeneity and spatial correlation of $\log_e K_s$, and local-scale dispersion), we made some simplifying assumptions. The first assumption we made is that the relation between bulk electrical conductivity, σ_b, and solute concentration, C, is constant over the ERT image plane. In reality, the σ_b-C relation is variable due to spatial variability in porosity and in microscale structure of the pore network, which both define the σ_b-C relation. Therefore an additional uncertainty in the ERT derived concentration images must be included. However, as long as the σ_b-C relation is linear the local calibration constants of the σ_b-C relation cancel out when normalized local concentrations are calculated (equation (17)). As a consequence, uncertainty about the local σ_b-C relation does not influence the maps of stream tube parameters, v_s and λ_s. This implies that the use of a stream tube model to interpret ERT monitored transport, to infer mixing and dilution

parameters, and to characterize the spatial variability of the hydraulic conductivity, effectively neutralizes uncertainty about the σ_b-C relation and its spatial variability. As far as the averaged concentrations in the image plane, $\langle C(x_1, t)\rangle$, are concerned, the effect of the uncertainty or spatial variability of the local σ_b-C relation is averaged out when the calibration constants of the σ_b-C relation are not correlated with the arrival time or dilution of the locally observed BTCs. This is similar to the approximation of the flux averaged concentrations $\langle C^f(x_1, t)\rangle$ by the volume averaged concentrations, which is based on the assumption that local water fluxes are not correlated with local concentrations. The uncertainty about $\langle C^f(x_1, t)\rangle$ due to spatial variability of the σ_b-C relation must be placed against the bias or uncertainty due to the unknown local water fluxes.

[48] The second assumption we made is that the solute plume that was monitored is "ergodic," i.e., representative for the transport process in all realizations of the hydraulic conductivity field. For the interpretation of the transport parameters derived from tracer breakthrough in an image plane using first-order approximations of the stochastic flow and transport equations, the observed transport process must be ergodic. Whether or not a solute plume can be considered to be ergodic depends on its lateral extent [e.g., *Dentz et al.*, 2000]. Plumes with a smaller lateral extent sample less of the heterogeneity of the aquifer and are therefore less representative for the transport process in all realizations of the hydraulic conductivity field. As a consequence, the agreement between first-order estimated and equivalent transport parameters, for example, $\langle\lambda_s(x_1)\rangle$ and $\rho_{v_s v_s}(\mathbf{x})$, derived from a solute plume in a single realization is expected to decrease with decreasing lateral extent of the solute plume. Since the lateral spreading of a solute plume due to spatial variability of water flow in a heterogeneous aquifer is small [e.g., *Dagan*, 1989], this implies that for real tracer experiments solute plumes with a wide lateral extent should be injected. In the numerical experiment, a slab with a uniform initial concentration was injected. In real tracer experiments, a tracer solution is injected in injections wells, which leads to an initially non uniform solute mass distribution in the aquifer. The injection in a well represents a boundary value problem in which the concentration of the inflowing water is defined and more solute mass is injected in regions with higher hydraulic conductivity. For the analysis of the local breakthrough on a reference plane, the effect of spatial variability of the solute mass in the injection plane is, similar to the local differences in the σ_b-C relation, cancelled out when normalized concentrations are calculated so that stream tube parameters v_s and λ_s are not influenced. For the equivalent dispersivity of the surface averaged BTC, λ_{eq}, *Vanderborght et al.* [1998] showed that the difference between boundary and initial value problems are neglected in first-order approximations of λ_{eq}, which implies that these differences are less important in aquifers with a smaller heterogeneity of $\log_e K_s$.

[49] Third, we restricted the measurement setup to a 2-D arrangement of electrodes, in line with the inversion of 2-D electrical conductivity fields. The fact that the 2-D approximation of a 3-D electrical conductivity distribution did not lead to considerable artifacts in the inverted conductivity images indirectly indicates that the collected ERT data sets did not contain much information about the electrical conductivity distribution in the direction perpendicular to the image plane. Therefore a 3-D arrangement of electrodes seems necessary to derive 3-D electrical conductivity and concentration distributions. 3-D spatiotemporal concentration distributions can be used to map hydraulic conductivities at the investigated site using geostatistically based inversion procedures, for example, using sequential linear estimation [*Harvey and Gorelick*, 1995; *Yeh et al.*, 1995; *Yeh and Liu*, 2000]. Geostatistically based inversion procedures can also be used to invert ERT data sets [*Yeh et al.*, 2002; *Liu and Yeh*, 2004]. These methods constrain the inversion procedures using spatial covariance functions that characterize the spatial structure of the inverted variable field. *Kitanidis* [1999] showed that the smoothness constraint commonly used to regularize the ERT inverse problem (as in (31)) corresponds with a specific spatial covariance function used in the geostatistically based inverse formulation. Therefore the geostatistical inversion approach offers the possibility to include a priori information about the structure of the medium through the spatial covariance functions. It also provides a framework to incorporate additional information about local-scale electrical and hydraulic state variables in the ERT inversion [*Yeh et al.*, 2002; *Liu and Yeh*, 2004]. Furthermore, it offers the possibility to combine inversion of electric and hydraulic state variables in a joint electric-hydraulic inversion scheme [e.g., *Yeh and Simunek*, 2002, Figure 2]. Although these geostatistically based inversion methods bear a huge potential, our study shows that the state-of-the-art inversion of ERT data sets in conjunction with an a posteriori interpretation using equivalent transport models also reveals valuable information about subsurface transport processes and the underlying hydraulic structure.

[50] Finally, we assumed that the aquifer heterogeneity could be represented using a second-order stationary Gaussian random field, which assumes that the spatial variability is fully characterized by the spatial covariogram or the two point covariance. The Gaussian spatial heterogeneity model maximizes the entropy of the random field for a given spatial covariance. This results in disconnected regions of extreme values [*Gomez-Hernandez and Wen*, 1998]. Especially for transport, the connectivity of hydraulically highly conductive regions is very important [e.g., *Zinn and Harvey*, 2003]. However, given the difficulties in determining the spatial covariance function of hydraulic properties accurately, the characterization of the connectivity of the hydraulic conductivity from direct measurements seems to pose even larger problems. In that view, monitoring of the spatiotemporal transport process is a viable alternative to determine this connectivity since the effect of the connectivity is strongly manifested in the transport process.

Appendix A

[51] The arrival time of a particle i at a point $\mathbf{x}$ in the aquifer can be written as follows:

$$\tau_i(\mathbf{x}) = \overline{\tau}(x_1) + \tau''(\mathbf{x}) + \tau_i'(\mathbf{x}) \tag{A1}$$

where $\overline{\tau}(x_1)$ is the average particle arrival time at a reference plane, $\tau''(\mathbf{x})$ is the deviation of the average particle arrival

time at location $\mathbf{x}$ in a given realization of the velocity field from the average arrival time at the reference plane, i.e., $\tau''(\mathbf{x}) = \overline{\tau}(\mathbf{x}) - \overline{\tau}(x_1)$, and $\tau_i'(\mathbf{x})$ is the deviation of the particle arrival time from the average arrival time at location $\mathbf{x}$ (in a given realization of the velocity field), i.e., $\tau_i'(\mathbf{x}) = \tau_i(\mathbf{x}) - \overline{\tau}(\mathbf{x})$. From their definition, it follows that the travel time deviations $\tau''(\mathbf{x})$, $\tau_i'(\mathbf{x})$, and $\tau_j'(\mathbf{x}')$ are mutually independent. The two-particle arrival time covariance $\sigma_{\tau\tau}(\mathbf{x}, \mathbf{x} + \mathbf{h})$, which is the covariance of arrival times of two different particles at locations $\mathbf{x}$ and $\mathbf{x} + \mathbf{h}$, is

$$\sigma_{\tau\tau}(\mathbf{x}, \mathbf{x}+\mathbf{h}) = \left\langle \left(\tau_i(\mathbf{x}) - \bar{\tau}(x_1)\right)\left(\tau_j(\mathbf{x}+\mathbf{h}) - \bar{\tau}(x_1)\right)\right\rangle = \langle \tau''(\mathbf{x})\tau''(\mathbf{x}+\mathbf{h})\rangle \quad \text{(A2)}$$

According to the definition of the stream tube velocity, $v_s(\mathbf{x})$ (equation (13)) and the particle travel time (equation (A1)) a first-order expansion of $v_s(\mathbf{x})$ is

$$v_s(\mathbf{x}) \approx \frac{x_1}{\overline{\tau}(x_1)} - \frac{x_1 \tau''(\mathbf{x})}{\overline{\tau}(x_1)^2} \quad \text{(A3)}$$

Using equation (A3), the first-order estimate of the expected stream tube velocity and the stream tube spatial covariance is

$$\langle v_s(\mathbf{x})\rangle \approx \frac{x_1}{\overline{\tau}(x_1)} = U_1 \quad \text{(A4)}$$

$$C_{v_s v_s}(\mathbf{x}, \mathbf{x}+\mathbf{h}) = \langle (v_s(\mathbf{x}) - \langle v_s(\mathbf{x})\rangle)(v_s(\mathbf{x}+\mathbf{h}) - \langle v_s(\mathbf{x}+\mathbf{h})\rangle)\rangle \approx \frac{x_1^2 \langle \tau''(\mathbf{x})\tau''(\mathbf{x}+\mathbf{h})\rangle}{\bar{\tau}(x_1)^4} \quad \text{(A5)}$$

Inserting equations (A2) and (A3) in equation (A5) leads to equation (25).

Notation

a	relative resistance error.
b	absolute resistance error (Ω).
c	time normalized concentrations (d^{-1}).
C	concentration (kg m^{-3}).
C_0	initial tracer concentration (kg m^{-3}).
C^f	flux or flux averaged concentration (kg m^{-3}).
C^r	resident or volume averaged concentration (kg m^{-3}).
C_{yy}	spatial covariance of variable y.
$\mathbf{d}$	data vector of $\log_e$ transformed transfer resistances.
D_0	molecular diffusion constant (m^2 d^{-1}).
$\mathbf{d_0}$	initial or reference data vector of $\log_e$ transformed transfer resistances.
$\mathbf{D_d}$	local-scale dispersion (m^2 d^{-1}).
$\mathbf{D_{eq}}$	equivalent dispersion (m^2 d^{-1}).
F	expected value of $\log_e$ transformed hydraulic conductivity.
$\mathbf{f}$	forward model operator of the Poisson equation.
f	perturbation of $\log_e$ transformed hydraulic conductivity.
$\mathbf{h}$	separation lag (m).
I	current strength (A).
$\mathbf{k}$	wave number (m^{-1}).
K_s	saturated hydraulic conductivity (m d^{-1}).
L	length of simulation domain (m).
$\mathbf{m}$	parameter vector of $\log_e$ transformed σ_b of the finite element grid.
$\mathbf{m_0}$	initial parameter vector of $\log_e$ transformed σ_b of the finite element grid.
Pe	Peclet number.
$\mathbf{q}$	Darcy flow velocity (m d^{-1}).
$\mathbf{q_s}$	solute flux (kg m^{-2} d^{-1}).
R	correlation coefficient.
$\mathbf{R}$	roughness matrix
r_i^k	transfer resistance for current injection at electrodes i and i + 2 and voltage measurements between electrodes k and k + 2 (Ω).
$S_{yy}(\mathbf{k})$	spectrum of variable y.
T_0	zeroth time moment of a breakthrough curve (kg m^{-3} d).
$\mathbf{U}$	large-scale uniform advection velocity (m d^{-1}).
$\mathbf{u}$	pore water velocity (m d^{-1}).
$\mathbf{v_d}$	dispersive velocity fluctuation (m d^{-1}).
v_s	stream tube velocity (m d^{-1}).
$\mathbf{W}$	matrix containing data weights.
$\mathbf{x}$	coordinate (m).
$\mathbf{X}(\tau, \mathbf{a})$	coordinate at time t of a particle that was released at point $\mathbf{a}$ (m).
$\mathbf{x_d}$	dispersive displacement (m).
α	regularization parameter.
β	parameter of the $\sigma_b - C$ calibration relation.
$\Delta(x_i)$	grid size (m).
δ	Dirac function.
δ_{ij}	Kronecker delta.
ε	zero-mean uncorrelated Gaussian noise.
ϕ_0	water-filled porosity.
γ_i	spatial correlation length in direction i (m).
φ_i	electric potential due to current injection at electrode i (V).
λ_{dL}	local-scale longitudinal dispersivity length (m).
λ_{dT}	local-scale transverse dispersivity length (m).
λ_{eq}	equivalent dispersivity (m).
λ_s	stream tube dispersivity (m).
ρ_{yy}	spatial correlation of variable y.
σ_b	bulk electrical conductivity(S m^{-1}).
$\sigma_{b,in}$	background bulk electrical conductivity (S m^{-1}).
$\sigma_{\tau\tau}(\mathbf{x}, \mathbf{x}+\mathbf{h})$	covariance of arrival times of two different particles at locations $\mathbf{x}$ and $\mathbf{x} + \mathbf{h}$ (d^2).
$\sigma_\tau^2(x_1)$	variance of particle arrival times at a reference plane at distance x_1 from the injection plane (d^2).
$\sigma_\tau^2(\mathbf{x})$	variance of particle arrival times at point $\mathbf{x}$ in a realisation of the conductivity field (d^2).
σ_y^2	variance of variable y.
$\tau(\mathbf{x})$	travel time of a particle from the injection plane to point $\mathbf{x}$ (d).
$\tau(\phi_0)$	tortuosity.
$\overline{\tau}(x_1)$	average of particle arrival times at a reference plane at distance x_1 from the injection plane (d).

$\bar{\tau}(\mathbf{x})$ average of particle arrival times at point $\mathbf{x}$ in a realisation of the conductivity field (d).

$\tau''(\mathbf{x})$ deviation of the average particle arrival time at location $\mathbf{x}$ in a given realization of the velocity field from the average arrival time at the reference plane (d).

$\tau_i'(\mathbf{x})$ deviation of the particle arrival time from the average arrival time at location $\mathbf{x}$ in a given realization of the velocity field (d).

ξ stream tube coordinate (m).

ψ hydraulic head (m).

Ψ objective function.

$\langle y \rangle$ expected value of y in all realizations of the hydraulic conductivity field or average of y in a plane perpendicular to the mean flow direction.

$\|\mathbf{y}\|$ L_2 norm of $\mathbf{y}$.

[52] **Acknowledgments.** Part of this work has been conducted in the frame of the EU funded ALERT project: Sustainable Management of Water Resources by Automated Real-Time Monitoring, contract GOCE-CT-2004-505329. We thank the Forschungszentrum Jülich for the allocated computing time on the CRAY T3E supercomputing system. We also gratefully acknowledge three reviewers, Andrew Binley, Partha Routh, and Jim Yeh, and the Associate Editor Lee Slater for their constructive and inspiring comments.

References

Bear, J. (1972), *Dynamics of Fluid in Porous Media*, Elsevier, New York.

Bellin, A., and Y. Rubin (2004), On the use of peak concentration arrival times for the inference of hydrogeological parameters, *Water Resour. Res.*, *40*, W07401, doi:10.1029/2003WR002179.

Bellin, A., P. Salandin, and A. Rinaldo (1992), Simulation of dispersion in heterogeneous porous formations: Statistics, first-order theories, convergence of computations, *Water Resour. Res.*, *28*, 2211–2227.

Binley, A., S. Henry-Poulter, and B. Shaw (1996), Examination of solute transport in an undisturbed soil column using electrical resistance tomography, *Water Resour. Res.*, *32*, 763–769.

Binley, A., G. Cassiani, R. Middleton, and P. Winship (2002), Vadose zone flow model parameterisation using cross-borehole radar and resistivity imaging, *J. Hydrol.*, *267*, 147–159.

Cirpka, O. A., and P. K. Kitanidis (2000), Characterization of mixing and dilution in heterogeneous aquifers by means of local temporal moments, *Water Resour. Res.*, *36*, 1221–1236.

Dagan, G. (1989), *Flow and Transport in Porous Formations*, Springer, New York.

Dagan, G., V. Cvetkovic, and A. Shapiro (1992), A solute flux approach to transport in heterogeneous formations. 1. The general framework, *Water Resour. Res.*, *28*, 1369–1376.

Daily, W. D., A. L. Ramirez, D. J. LaBrecque, and J. Nitao (1992), Electrical resistivity tomography of vadose water movement, *Water Resour. Res.*, *28*, 1429–1442.

Dentz, M., H. Kinzelbach, S. Attinger, and W. Kinzelbach (2000), Temporal behavior of a solute cloud in a heterogeneous porous medium: 2. Spatially extended injection, *Water Resour. Res.*, *36*, 3605–3614.

Dey, A., and H. F. Morrison (1979), Resistivity modeling for arbitrarily shaped 3-dimensional structures, *Geophysics*, *44*, 753–780.

Ezzedine, S., Y. Rubin, and J. Chen (1999), Bayesian method for hydrogeological site characterization using borehole and geophysical survey data: Theory and application to the Lawrence Livermore National Laboratory Superfund site, *Water Resour. Res.*, *35*, 2671–2683.

Fiori, A. (1996), Finite Peclet extensions of Dagan's solution to transport in anisotropic heterogeneous formations, *Water Resour. Res.*, *32*, 193–198.

Fiori, A., and G. Dagan (1999), Concentration fluctuations in transport by groundwater: Comparison between theory and field experiments, *Water Resour. Res.*, *35*, 105–112.

Fiori, A., and G. Dagan (2000), Concentration fluctuations in aquifer transport. A rigorous first-order solution and applications, *J. Contam. Hydrol.*, *45*, 139–163.

French, H. K., C. Hardbattle, A. Binley, P. Winship, and L. Jakobsen (2002), Monitoring snowmelt induced unsaturated flow and transport using electrical resistivity tomography, *J. Hydrol.*, *267*, 273–284.

Gelhar, L. W. (1993), *Stochastic Subsurface Hydrology*, Prentice-Hall, Upper Saddle River, N. J.

Gomez-Hernandez, J. J., and X.-H. Wen (1998), To be or not to be multi-Gaussian? A reflection on stochastic hydrogeology, *Adv. Water Resour.*, *21*, 47–61.

Harvey, C. F., and S. M. Gorelick (1995), Mapping hydraulic conductivity: Sequential conditioning with measurements of solute arrival time, hydraulic-head, and local conductivity, *Water Resour. Res.*, *31*, 1615–1626.

Hubbard, S. S., and Y. Rubin (2004), Hydrogeophysics overview, in *Hydrogeophysics*, edited by Y. Rubin and S. S. Hubbard, pp. 3–21, Springer, New York.

Hubbard, S. S., Y. Rubin, and E. Majer (1999), Spatial correlation structure estimation using geophysical and hydrogeological data, *Water Resour. Res.*, *35*, 1809–1825.

Jury, W. A., and G. Sposito (1985), Field calibration and validation of solute transport models for the unsaturated zone, *Soil Sci. Soc. Am. J.*, *49*, 1331–1341.

Kapoor, V., and P. K. Kitanidis (1998), Concentration fluctuations and dilution in aquifers, *Water Resour. Res.*, *34*, 1181–1193.

Kemna, A. (2000), *Tomographic Inversion of Complex Resistivity: Theory and Application*, Der Andere, Osnabrück, Germany.

Kemna, A., J. Vanderborght, B. Kulessa, and H. Vereecken (2002), Imaging and characterisation of subsurface solute transport using electrical resistivity tomography (ERT) and equivalent transport models, *J. Hydrol.*, *267*, 125–146.

Kitanidis, P. K. (1999), Generalized covariance functions associated with the Laplace equation and their use in interpolation and inverse problems, *Water Resour. Res.*, *35*, 1361–1367.

Kraichnan, R. H. (1970), Diffusion by a random velocity field, *Phys. Fluids*, *13*, 22–31.

LaBrecque, D. J., and S. H. Ward (1990), Two-dimensional cross-borehole resistivity model fitting, in *Geotechnical and Environmental Geophysics*, vol. III, edited by S. H. Ward, pp. 51–74, Soc. of Explor. Geophys., Tulsa, Okla.

LaBrecque, D. J., and X. Yang (2001), Difference inversion of ERT data: A fast inversion method for 3D in situ monitoring, *J. Environ. Eng. Geophys.*, *5*, 83–90.

LaBrecque, D. J., M. Miletto, W. D. Daily, A. L. Ramirez, and E. Owen (1996), The effects of noise on Occam's inversion of resistivity tomography data, *Geophysics*, *61*, 538–548.

Lesmes, L., and S. Friedman (2004), The relationships between the electrical and hydrological properties of rocks and soil, in *Hydrogeophysics*, edited by Y. Rubin and S. S. Hubbard, pp. 87–128, Springer, New York.

Liu, S., and T.-C. J. Yeh (2004), An integrative approach for monitoring water movement in the vadose zone, *Vadose Zone J.*, *3*, 681–692.

Morelli, G., and D. J. LaBrecque (1996), Advances in ERT modeling, *Eur. J. Environ. Eng. Geophys.*, *1*, 171–186.

Neuendorf, O. (1997), *Numerische 3D-Simulation des Stofftransports in einem heterogenen Aquifer*, report, Forschungszentrum Jülich GmbH, Jülich, Germany.

Pannone, M., and P. K. Kitanidis (1999), Large-time behavior of concentration variance and dilution in heterogeneous formations, *Water Resour. Res.*, *35*, 623–634.

Parker, J. C., and M. T. Van Genuchten (1984), Flux-averaged and volume-averaged concentrations in continuum approaches to solute transport, *Water Resour. Res.*, *20*, 866–872.

Purvance, D. T., and R. Andricevic (2000), Geoelectric characterization of the hydraulic conductivity field and its spatial structure at variable scales, *Water Resour. Res.*, *36*, 2915–2924.

Rubin, Y., and S. Ezzedine (1997), The travel time of solutes at the Cape Cod tracer experiment: Data analysis, modeling, and structural parameter inference, *Water Resour. Res.*, *33*, 1537–1547.

Rubin, Y., G. Mavko, and J. Harris (1992), Mapping permeability in heterogeneous aquifers using hydraulic and seismic data, *Water Resour. Res.*, *28*, 1809–1816.

Russo, D. (1995), On the velocity covariance and transport modeling in heterogeneous anisotropic porous formations: 1. Saturated flow, *Water Resour. Res.*, *31*, 129–137.

Singha, K., A. M. Binley, J. W. Lane Jr., and S. M. Gorelick (2003), Electrical imaging of tracer migration at the Massachusetts Military Reservation, Cape Cod, in *Symposium on the Application of Geophysics to Engineering and Environmental Problems* (*SAGEEP*), *April 6–10, 2003, San Antonio, Texas, Proceedings* [CD-ROM], 464–474, Environ. and Eng. Geophys. Soc., Denver, Colo.

Slater, L., and D. P. Lesmes (2002), Electrical-hydraulic relationships for unconsolidated sediments, *Water Resour. Res.*, *38*(10), 1213, doi:10.1029/2001WR001075.

Slater, L., A. Binley, and D. Brown (1997), Electrical imaging of fractures using ground-water salinity change, *Ground Water*, *35*, 436–442.

Slater, L., A. Binley, W. D. Daily, and R. Johnson (2000), Cross-hole electrical imaging of a controlled saline tracer injection, *J. Appl. Geophys.*, *44*, 85–102.

Spitzer, K. (1998), The three-dimensional dc sensitivity for surface and subsurface sources, *Geophys. J. Int.*, *134*, 736–746.

Vanderborght, J. (2001), Concentration variance and spatial covariance in second-order stationary heterogeneous conductivity fields, *Water Resour. Res.*, *37*, 1893–1912.

Vanderborght, J., and H. Vereecken (2001), Analyses of locally measured bromide breakthrough curves from a natural gradient tracer experiment at Krauthausen, *J. Contam. Hydrol.*, *48*, 23–43.

Vanderborght, J., and H. Vereecken (2002), Estimation of local scale dispersion from local breakthrough curves during a tracer test in a heterogeneous aquifer: The Lagrangian approach, *J. Contam. Hydrol.*, *54*, 141–171.

Vanderborght, J., D. Mallants, and J. Feyen (1998), Solute transport in a heterogeneous soil for boundary and initial conditions: Evaluation of first-order approximations, *Water Resour. Res.*, *34*, 3255–3270.

Vereecken, H., G. Lindenmayr, O. Neuenedorf, U. Döring, and R. Seidemann (1994), TRACE: A mathematical model for reactive transport in 3D variable saturated porous media, *ICG-4 Int. Rep. 501494*, Forschungszentrum Jülich GmbH, Jülich, Germany.

Woodbury, A. D., and Y. Rubin (2000), A full-Bayesian approach to parameter inference from tracer travel time moments and investigation of scale effects at the Cape Cod experimental site, *Water Resour. Res.*, *36*, 159–171.

Yeh, T. C. J., and S. Y. Liu (2000), Hydraulic tomography: Development of a new aquifer test method, *Water Resour. Res.*, *36*, 2095–2105.

Yeh, T.-C. J., and J. Simunek (2002), Stochastic fusion of information for characterizing and monitoring the vadose zone, *Vadose Zone J.*, *1*, 207–221.

Yeh, T. C. J., A. L. Gutjahr, and M. G. Jin (1995), An iterative cokriging-like technique for groundwater-flow modelling, *Ground Water*, *33*, 33–41.

Yeh, T. C. J., S. Liu, R. J. Glass, K. Baker, J. R. Brainard, D. Alumbaugh, and D. LaBrecque (2002), A geostatistically based inverse model for electrical resistivity surveys and its applications to vadose zone hydrology, *Water Resour. Res.*, *38*(12), 1278, doi:10.1029/2001WR001204.

Zinn, B., and C. F. Harvey (2003), When good statistical models of aquifer heterogeneity go bad: A comparison of flow, dispersion, and mass transfer in connected and multivariate Gaussian hydraulic conductivity fields, *Water Resour. Res.*, *39*(3), 1051, doi:10.1029/2001WR001146.

H. Hardelauf, A. Kemna, J. Vanderborght, and H. Vereecken, Agrosphere Institute, ICG-IV, Forschungszentrum Jülich GmbH, D-52425 Jülich, Germany. (j.vanderborght@fz-juelich.de)